The relationship between the global mean deep-sea and surface temperature during the Early Eocene

Barbara Goudsmit[1,1], Angelique Lansu[2,2], Michiel Baatsen[3,3], Anna S. von der Heydt[4,4], Niels Jonathan de Winter[5,5], Yurui Zhang[6,6], Ayako Abe-Ouchi[7,7], Agatha Margaretha De Boer[8,8], Wing-Le Chan[7,7], Yannick Donnadieu[9,9], David Hutchinson[10,10], Gregor Knorr[11,11], Jean-Baptiste Ladant[12,12], Polina A Morozova[13,13], Igor Niezgodzki[14,14], Sebastian Steinig[15,15], Aradhna Tripati[16,16], Zhongshi Zhang[17,17], Jiang Zhu[18,18], and Martin Ziegler[3,3]

[1]Royal Netherlands Institute for Sea Research
[2]Open Universiteit
[3]Utrecht University
[4]Institute for Marine and Atmospheric research Utrecht, Utrecht University
[5]Vrije Universiteit Brussel
[6]Xiamen University
[7]University of Tokyo
[8]Stockholm University
[9]Centre national de la recherche scientifique
[10]University of New South Wales
[11]AWI Bremerhaven
[12]Laboratoire des Sciences du Climat et de l'Environnement
[13]Institute of Geography, Russian Academy of Sciences
[14]ING PAN - Institute of Geological Sciences Polish Academy of Sciences
[15]University of Bristol
[16]University of California,Los Angeles
[17]Bjerknes Centre for Climate Research
[18]National Center for Atmospheric Research

November 30, 2022

Abstract

Our current understanding of global mean near-surface (land and sea) air temperature (GMSAT) during the Cenozoic era relies on paleo-proxy estimates of deep-sea temperature combined with assumed relationships between global mean deep-sea temperature (GMDST), global mean sea-surface temperature (GMSST), and GMSAT. The validity of these assumptions is essential in our understanding of past climate states such as the Early Eocene Climate Optimum hothouse climate (EECO, 56–48 Ma). The EECO remains relevant today, because EECO-like CO_2 levels are possible in the 22nd century under continued high CO_2 emissions. We analyze the relationship between the three global temperature indicators for the EECO using 25 different millennia-long model simulations with varying CO_2 levels from the Deep-Time Model Intercomparison Project (DeepMIP). The model simulations show limited spatial variability in deep-sea temperature, indicating that local temperature estimates can be regarded representative of GMDST. Linear regression analysis indicates that compared to GMSST, both GMDST and GMSAT respond more strongly to changes in atmospheric CO_2 by factors of 1.18 and 1.17, respectively. Consequently, this model-based analysis validates the assumption that changes in GMDST can be used to estimate changes in GMSAT during

the EECO. Paleo-proxies of GMDST, GMSST, and GMSAT during EECO show the best fit with model simulations having an atmospheric CO2 level of 1,680 ppm, which matches paleo-proxies of atmospheric CO2 during EECO. Similar analyses of other past climate states are needed to examine whether these results are robust throughout the Cenozoic, providing insight into the long-term future warming under various shared socioeconomic pathways.

Hosted file

`goudsmit_et_al_deepmip_suppinfo.docx` available at https://authorea.com/users/559269/articles/608208-the-relationship-between-the-global-mean-deep-sea-and-surface-temperature-during-the-early-eocene

Barbara Goudsmit-Harzevoort[1,2], Angelique Lansu[3], Michiel L. J. Baatsen[4], Anna S. von der Heydt[4], Niels J. de Winter[2,5], Yurui Zhang[6], Ayako Abe-Ouchi[7], Agatha de Boer[8], Wing-Le Chan[7], Yannick Donnadieu[9], David K. Hutchinson[10], Gregor Knorr[11], Jean-Baptiste Ladant[12], Polina Morozova[13], Igor Niezgodzki[14], Sebastian Steinig[15], Aradhna Tripati[16], Zhongshi Zhang[17,18], Jiang Zhu[19], & Martin Ziegler[2]

[1] Department of Estuarine & Delta Systems, NIOZ Royal Netherlands Institute for Sea Research, 't Horntje, The Netherlands.

[2] Department of Earth Sciences, Utrecht University, Utrecht, The Netherlands.

[3] Department of Environmental Sciences, Open Universiteit, Heerlen, The Netherlands.

[4] IMAU Institute for Marine and Atmospheric Research, Department of Physics, Utrecht University, Utrecht, The Netherlands.

[5] AMGC Research Group, Vrije Universiteit Brussel, Brussels, Belgium.

[6] State Key Laboratory of Marine Environmental Science, College of Ocean & Earth Sciences, Xiamen University, Xiamen, China.

[7] Atmosphere and Ocean Research Institute, The University of Tokyo, Kashiwa, Japan.

[8] Department of Geological Sciences, Bolin Centre for Climate Research, Stockholm University, Stockholm, Sweden.

[9] Aix-Marseille Université, CNRS, IRD, INRAE, Collège de France, CEREGE, Aix-en-Provence, France.

[10] Climate Change Research Centre, University of New South Wales, Sydney, Australia.

[11] Alfred Wegener Institute, Helmholtz Centre for Polar and Marine Research, Bremerhaven, Germany.

[12] Laboratoire des Sciences du Climat et de l'Environnement, LSCE/IPSL, UMR 8212, CEA-CNRS-UVSQ, Université Paris-Saclay, Gif-sur-Yvette, France.

[13] Institute of Geography, Russian Academy of Sciences, Moscow, Russia.

[14] ING PAN - Institute of Geological Sciences Polish Academy of Sciences, Research Center in Kraków, Biogeosystem Modelling Group, Kraków, Poland.

[15] School of Geographical Sciences, University of Bristol, Bristol, UK.

[16] Department of Earth, Planetary, and Space Science, Department of Atmospheric and Oceanic Science, Institute of the Environment and Sustainability, American Indian Studies Center, Center for Diverse Leadership in Science, University of California, Los Angeles, Los Angeles, USA.

[17]Department of Atmospheric Science, School of Environmental studies, China University of Geoscience, Wuhan, China.

[18]NORCE Norwegian Research Centre, Bjerknes Centre for Climate Research, Bergen, Norway.

[19]Climate and Global Dynamics Laboratory, National Center for Atmospheric Research, Boulder, Colorado, USA.

Corresponding authors: Barbara Goudsmit-Harzevoort (barbara.goudsmit-harzevoort@nioz.nl) and Martin Ziegler (`m.ziegler@uu.nl`)

Key Points:

- Based on 25 Early Eocene model simulations (DeepMIP), the global mean deep-sea and surface temperature are approximately equally sensitive to changes in atmospheric CO_2.

- There is limited spatial variability in deep-sea temperature in these simulations, making local deep-sea temperature estimates generally representative of the global mean.

- The model simulations with a CO_2 forcing of 1,680 ppm align well with paleo-proxies in the combination of global mean deep-sea, sea-surface, and surface temperature.

Abstract

Our current understanding of global mean near-surface (land and sea) air temperature (GMSAT) during the Cenozoic era relies on paleo-proxy estimates of deep-sea temperature combined with assumed relationships between global mean deep-sea temperature (GMDST), global mean sea-surface temperature (GMSST), and GMSAT. The validity of these assumptions is essential in our understanding of past climate states such as the Early Eocene Climate Optimum hothouse climate (EECO, 56–48 Ma). The EECO remains relevant today, because EECO-like CO_2 levels are possible in the 22nd century under continued high CO_2 emissions. We analyze the relationship between the three global temperature indicators for the EECO using 25 different millennia-long model simulations with varying CO_2 levels from the Deep-Time Model Intercomparison Project (DeepMIP). The model simulations show limited spatial variability in deep-sea temperature, indicating that local temperature estimates can be regarded representative of GMDST. Linear regression analysis indicates that compared to GMSST, both GMDST and GMSAT respond more strongly to changes in atmospheric CO_2 by factors of 1.18 and 1.17, respectively. Consequently, this model-based analysis validates the assumption that changes in GMDST can be used to estimate changes in GMSAT during the EECO. Paleo-proxies of GMDST, GMSST, and GMSAT during EECO show the best fit with model simulations having an atmospheric CO_2 level of 1,680 ppm, which matches paleo-proxies of atmospheric CO_2 during EECO. Similar analyses of other past climate states are needed to examine whether these results are robust throughout the

Cenozoic, providing insight into the long-term future warming under various shared socioeconomic pathways.

Plain Language Summary

A widely used indicator of global climate change is the change in global mean (land and sea) surface air temperature (GMSAT). Our current understanding of the GMSAT evolution during the last 66 million years is largely based on deep-sea temperature proxies from fossilized micro-organisms and the assumption that changes in the global mean deep-sea temperature (GMDST) are similar to those in GMSAT. In short, GMDST and GMSAT are linked via the global mean sea-surface temperature (GMSST) by assuming that they are both less sensitive than the GMSST to atmospheric CO_2 changes by the same degree. The validity of this assumption is essential in our understanding of past climate states such as the Early Eocene Climate Optimum (EECO, 56–48 million years ago), a hothouse period characterized by high atmospheric CO_2 levels. We analyzed the relationship between the three global temperature indicators in climate model simulations of the EECO. Based on linear regression analysis, we find that changes in GMDST can indeed be used to estimate changes in GMSAT during the EECO (regression slope 0.99). Furthermore, paleo-proxies of GMDST, GMSST, and GMSAT during EECO show the best fit with the model simulations having an atmospheric CO_2 level of 1,680 ppm, which matches paleo-proxies of atmospheric CO_2 during EECO. This indicates a good fit between models and proxy-data.

1 Introduction

The atmospheric CO_2 concentration has fluctuated considerably over the Cenozoic era (66 Ma – present) (Figure 1; Rae et al., 2021). During the Early Eocene Climate Optimum (EECO, 56–48 Ma) – the warmest interval of the Cenozoic – the atmospheric CO_2 concentration reached values between 1,150 and 2,000 ppm (Anagnostou et al., 2020; Rae et al., 2021). After the EECO hothouse climate, the atmospheric CO_2 level gradually declined and remained below 1,000 ppm for the remainder of the Cenozoic (Gulev et al., 2021). In the more recent past, the atmospheric CO_2 concentration has increased from 280 ppm at the start of the industrial era around 1750 AD to 412.5 ppm in 2020 (NOAA, 2021). In its Sixth Assessment Report (AR6), the Intergovernmental Panel on Climate Change (IPCC) considers five main scenarios for the future atmospheric CO_2 level based on a set of Shared Socioeconomic Pathways (SSPs). In case of continued high CO_2 emissions (SSP5-8.5), the atmospheric CO_2 concentration can reach values above 1,100 ppm by 2100, leveling off at 2,200 ppm between 2200 and 2250; comparable to the level during the EECO (Figure 1; Cheng et al., 2021). This makes the climate of the EECO of interest today, to gain understanding of how the climate system operates under these possible extreme future CO_2 levels (Burke et al., 2018; Tierney et al., 2020).

Compared to today, the world during the Early Eocene displays some striking differences (Figure 1 (a) and (b)). There were no ice sheets on Antarctica and

Greenland (Zachos et al., 2001), and frost-free winters allowed forest growth in polar regions (Pross et al., 2012). The North-Atlantic Ocean was narrower than nowadays, limiting the connectivity with the Arctic Ocean. Furthermore, the oceanic gateway between Antarctica and Australia was more restrictive compared to today (Lunt et al., 2021; Sauermilch et al., 2021). These differences in land cover and continental configuration also provide a climate forcing, in addition to the higher atmospheric CO_2 level. Furthermore, the EECO represents a quasi-equilibrated hothouse climate state (Figure 1 (c)), while the climate of the 21st century is still in transient state due to the pronounced CO_2 rise in a relatively short time (Figure 1 (d)). Although the EECO does not represent a direct analogue for future climate scenarios due to these differences, reconstructions of the EECO climate can deepen our understanding of the operational modes in a climate system under high CO_2 conditions.
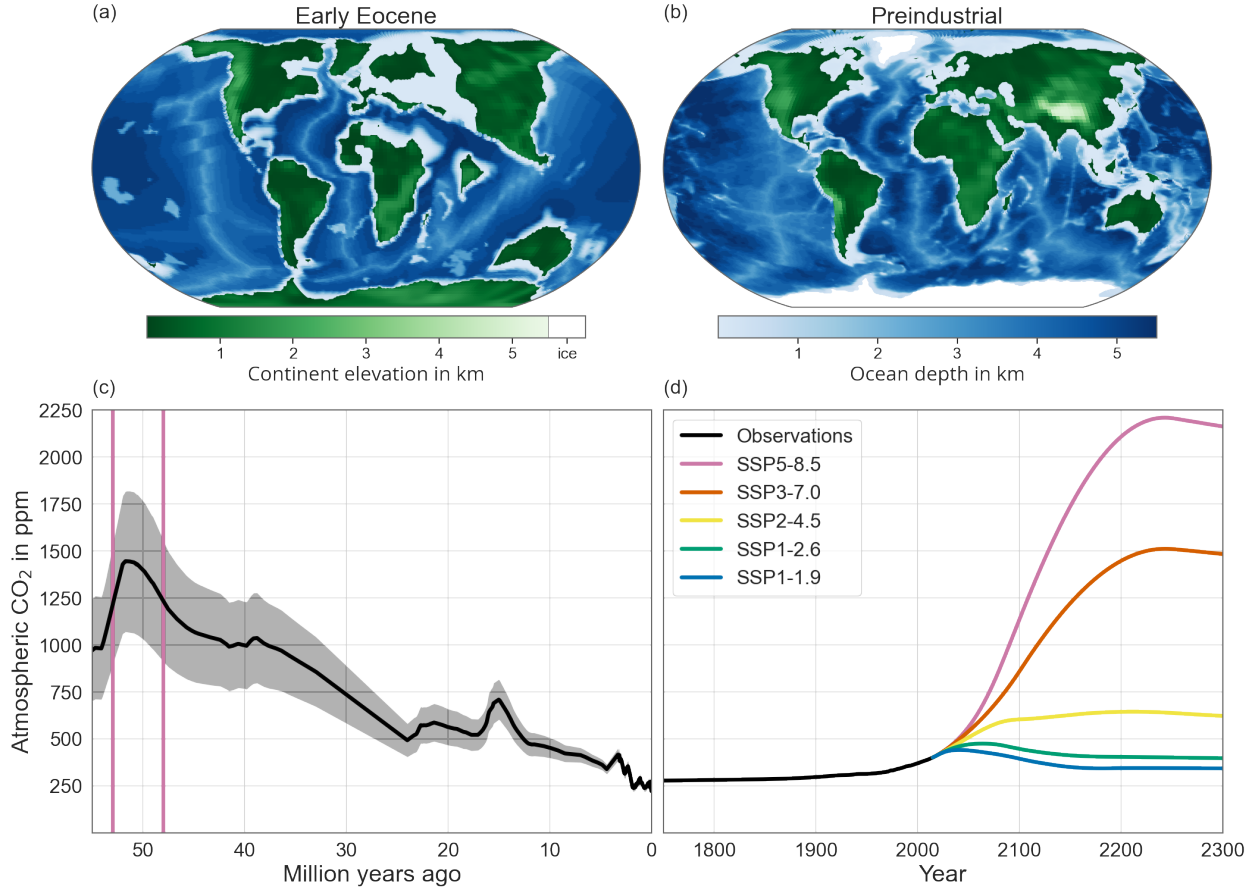

Figure 1. Top: Continental configuration during the Early Eocene (a) and the Preindustrial (b) with shared color bars for continent elevation and ocean depth. Ice sheets during the Preindustrial are depicted in white. Bottom: Evolution

4

of the atmospheric CO_2 concentration in ppm during the last 55 million years (c) with uncertainty in shading, based on data from Rae et al. (2021), and for 1750-2014 and 2015-2300 (d) based on respectively observations and the five scenarios used in IPCC Assessment Report 6 (Chen et al., 2021), based on data from The University of Melbourne (n.d.).

An important indicator of both past climate states like the EECO and scenarios of the future climate is the global mean surface air temperature (GMSAT): the mean near-surface air temperature above both land and sea. Current insights into the GMSAT evolution during the Cenozoic era, as presented in IPCC AR6 (Gulev et al., 2021), are based on estimates of deep-sea temperature (DST) from oxygen isotope compositions of benthic foraminifera (Hansen et al., 2013; Westerhold et al., 2020). This ^{18}O paleothermometry is based on the temperature-dependent fractionation of the oxygen isotopes ^{16}O and ^{18}O in the calcium carbonate shells of these micro-organisms (Urey, 1948; McCrea, 1950). The DST estimates are translated into GMSAT estimates by assuming a 1-on-1 relationship between changes in GMDST and GMSAT prior to the Pliocene using the following line of reasoning of Hansen et al (2013):

1. The GMDST is essentially determined by the sea surface temperature (SST) at high-latitude sites of deep-water formation, where surface water sinks to the bottom. Hence, GMDST exhibits the same sensitivity to CO_2 changes as the high-latitude SST,

2. Due to polar amplification, the high-latitude SST, and hence also GMDST, responds stronger to CO_2 changes than the global mean SST (GMSST),

3. The surface temperature change is greater over land than over ocean. Hence, GMSAT responds stronger to CO_2 changes than GMSST,

4. GMDST and GMSAT are equally sensitive to CO_2 changes, when assuming that GMSST underestimates the sensitivities of GMDST and GMSAT by the same factor.

The validity of these underlying assumptions is essential to our understanding of past and future climate states under hothouse conditions. In this light, Valdes et al. (2021) used climate model simulations of different time-periods covering the whole Phanerozoic era to investigate the relationship between DST and GMSAT. They found an overall linear relationship between DST and GMSAT during the Phanerozoic, yet with variable slope and coefficient of determination depending on the geologic time-period under consideration. To build on this analysis, we investigated the relationships between GMDST, GMSST, and GMSAT for one specific time-period during the Cenozoic: the EECO. We use an ensemble of model simulations of the EECO climate assuming different atmospheric CO_2 levels, performed as part of the Deep-Time Model Intercomparison Project (DeepMIP) (Lunt et al., 2017; 2021). Hence, we analyze the temperature relationships under fixed non-CO_2 climatic factors (such as continental configuration and astronomical conditions) and variable CO_2 level.

In addition to this model-based analysis, we performed a model-data comparison to investigate the alignment between the model estimates and paleo-proxy based reconstructions of atmospheric CO_2 level, GMDST, GMSST, and GMSAT during the EECO. Previous EECO model simulations required atmospheric CO_2 levels as high as 4,480 ppm (16 times the preindustrial (PI) level) to reproduce paleo-proxies of surface temperatures (Lunt et al., 2012). For the DeepMIP model simulations, Lunt et al. (2021) found that the simulations with CO_2 levels of 1,120 (4 times PI) and 1,680 ppm (6 times PI) are most consistent with paleo-proxies of GMSAT and CO_2 level during the EECO. In our analysis, we additionally consider paleo-proxies of GMDST and GMSST and analyze the model-data alignment for the combination of the three global mean temperature indicators and the CO_2 levels.

2 Data

2.1 Output of EECO model simulations

As part of the DeepMIP, simulations for the EECO were performed with nine Earth System Models based on a standard set of boundary conditions (Lunt et al., 2017; 2021). Each model performed a preindustrial control run, and several EECO simulations at various atmospheric CO_2 concentrations ranging from the PI CO_2 concentration of 280 ppm to 9 times this baseline (2,520 ppm; Table 1). Most model simulations ran for at least 2,000 years, allowing us to analyze a long-term response of the deep-sea and surface temperatures to the atmospheric CO_2 concentration. The model simulation output data contain monthly averages of variables over the last 100 simulation years on the model-specific grid (Table 2), except for the NorESM ocean variables which are available as annual instead of monthly averages.

Table 1. Large-scale features of the DeepMIP simulations per model (Lunt et al., 2021). The resolution presented for the ocean grid is the nominal resolution, as most models use a non-rectangular grid for their ocean component (such as a bipolar, tripolar, or displaced pole grid). The depth levels of all models vary with thickness and become thicker with increasing depth. Note that several models start with 1 run and branch off other runs after a spin up period. The run-time presented is the total run-time, including possible spin-up. Detailed information on the simulations of each model is provided in (Lunt et al., 2021). Additionally, (Zhu et al., 2019) and (Zhang et al., 2020) serve as references for the DeepMIP simulations of CESM and IPSL respectively. The models are referred to by the specified short name in the remainder of this article.

Model	Short name	Simulations in multiplication factor CO_2	Ocean resolution in latitude x longitude, depth levels	Atmosphere resolution in latitude x longitude, vertical levels	Run time in years
CESM1.2_ CAM5	CESM	, 3, 6, 9 + PI	° x 1°, 60 depth levels	° x 2.5°, 30 vertical levels	,600 (1xCO_2) 2,000 (others)
COSMOS-landveg_r2413	COSMOS	, 3, 4 + PI	° x 3.0°, 40 depth levels	° x 3.75°, 19 vertical levels	,500
GFDL_CM2.1	GFDL	, 2, 3, 4, 6 + PI	° x 1.5°, 50 depth levels	° x 3.75°, 24 vertical levels	,000
HadCM3B-M2.1aN	HadCM High Resolution	, 2, 3 + PI	° x 1.25°, 20 depth levels	° x 3.75°, 19 vertical levels	,500
HadCM3BL-M2.1aN	HadCM Low Resolution	, 2, 3 + PI	° x 3.75°, 20 depth levels	° x 3.75°, 19 vertical levels	,500
INM-CM4-8	INMCM	+ PI	° x 1°, 33 depth levels	° x 2°, 17 vertical levels	,150
IPSL-CM5A2	IPSL	, 3 + PI	-2° x 2°, 31 depth levels	° x 2.5°, 39 vertical levels	,000
MIROC4m	MIROC	, 2, 3 + PI	-1.4° x 1.4°, 44 depth levels	° x 2.8°, 20 vertical levels	,000
NorESM1-F	NorESM	, 4 + PI	° x 1°, 70 depth levels	° x 2°, 26 vertical levels	,100

Table 2. DeepMIP variables used in the analysis. Temperatures in K are converted to °C by subtracting 273.15.

Variable	Model component	Name in data	Unit	Dimensions
Potential sea temperature	Ocean	thetao	°C	Month Latitude Longitude Depth level
Sea surface temperature	Ocean	tos	°C	Month Latitude Longitude
Near-surface air temperature	Atmosphere	tas	°C	
Top-of-atmosphere (TOA) outgoing longwave radiation (LW↑)	Atmosphere	rlut	W/m^2	
TOA outgoing shortwave radiation (SW↑)	Atmosphere	rsut	W/m^2	
TOA incoming shortwave radiation (SW↓)	Atmosphere	rsdt	W/m^2	

2.2 Data of modern ocean temperature

In order to compare the relationship between global temperature indicators during EECO with the modern climate, estimates of present-day GMDST, GMSST, and GMSAT were added as a reference in the analysis. Estimates of modern GMDST and GMSST were obtained from three datasets of global current ocean temperature data:

- Monthly values for January 2019 – December 2019 of the Global Ocean Physics Reanalysis GLORYS12V1 (short name GLORYS) dataset (E.U. Copernicus Marine Service Information, 2021b).

- Monthly values for January 2019 – December 2019 of the Multi Observation Global Ocean ARMOR3D (short name ARMOR) dataset (E.U. Copernicus Marine Service Information, 2021c).

- Quarterly values for Q1 2019 – Q4 2020 of the Global Ocean OSTIA Sea Surface Temperature (short name OSTIA) dataset (E.U. Copernicus Marine Service Information, 2021a). This dataset only supplies SST data.

An estimate of modern GMSAT was derived from monthly values for January 2016 – December 2020 of the ERA5 reanalysis dataset. The variable used to derive the GMSAT is the temperature of air at 2 m above the surface of land, sea or inland waters (Hersbach et al, 2019). An overview of the data used per dataset is given in Table S1.

2.3 EECO paleo-proxies

For the paleo-proxy estimates of GMDST, GMSST, GMSAT and CO_2 level during EECO, several existing proxy compilations were used. As a basis for our own estimates of GMSAT and GMSST, we used the dataset with marine and terrestrial surface temperature proxies compiled as part of DeepMIP (Hollis et al., 2019) as given in the supplementary information of (Inglis et al., 2020). The 27 marine temperature estimates in this set are based on four distinct methods for paleothermometry: stable oxygen isotope ratio (^{18}O; 5 estimates), Mg/Ca ratio (6 estimates), clumped isotopes (Δ_{47}; 5 estimates), and TEX_{86} (11 estimates). The first three methods infer surface temperature from the calcium carbonate shells of planktic foraminifera, while TEX_{86} relies on membrane lipid structures of thaumarchaeota, micro-organisms that dwell predominantly at the (sub-) surface (Hollis et al., 2019; and references therein). The 70 compiled proxies for terrestrial air temperature are based on membrane lipid structures produced by bacteria (22 estimates), Δ_{47} on soil carbonates (3 estimates), and analysis of fossil leaves (38 estimates) and pollen (7 estimates) (Hollis et al., 2019; and references therein). To derive proxy-based estimate of GMSST and GMSAT, we respectively used only the marine proxy estimates and both the marine and terrestrial estimates. Note that the full DeepMIP dataset additionally contains 7 marine estimates based on recrystallized planktonic foraminifera and 10 terrestrial estimates based on mammal and paleosol analysis. We did not include these estimates in the analysis, following the data selection choices of Inglis et al. (2020). The dataset provides all temperature estimate in °C (as the 50% percentile, i.e., median, of the temperature estimate derived from the proxy value) together with the location of the proxy specified by latitude and longitude during EECO (52 Ma) using a mantle reference frame (Inglis et al., 2020). An overview of the local SST and SAT proxies is given in Table S2 and the location of the proxies is depicted in Figure S1.

For a proxy-based estimate of GMDST, two additional estimates of GMSAT, and an estimate of atmospheric CO_2 level, we relied on literature. The paleo-proxy range for GMDST during EECO used in our analysis is based on the recent Δ_{47} analysis from Meckler et al. (2022). The temperature estimates for the EECO in this study are from the Newfoundland Margin in the North-Atlantic with paleo-depth 3,050 m and the Walvis Ridge in the South-Atlantic with paleo-depth 1,500. We chose a GMDST estimate based on Δ_{47} paleothermometry, because clumped isotope analysis has the advantage that no assumption needs

9

to be made regarding the ^{18}O of seawater, unlike ^{18}O analysis (Eiler, 2007; Ghosh et al., 2006). Regarding GMSAT, we used the estimated ranges from Inglis et al. (2020) and Zhu et al. (2019), both based on a combination of all marine and terrestrial methods of paleothermometry. Finally, the range for atmospheric CO_2 level during the EECO is based on the studies of Anagnostou et al. (2020) and Rae et al. (2021). Both constrain the atmospheric CO_2 level from the pH-dependent boron isotope composition in foraminifera together with the relationship between seawater's pH-level and carbonate chemistry.

3 Methods

3.1 Estimation of GMDST, GMSST, and GMSAT

The GMDST per model simulation is estimated using the monthly mean potential sea water temperature data (Table 2). The annual mean per grid cell was calculated as the average over the 12 months for all models except NorESM. We defined the deep-sea as the part of the ocean ranging from a depth of 2,000 m to the ocean floor. As most model depth levels do not exactly coincide with this boundary, we used a model-specific deep-sea definition starting at the depth level closest to 2,000 m (Table S3). The local DST per 2-dimensional (longitude, latitude) surface grid cell was calculated as the weighted average temperature of the column of grid cells ranging from the model-specific deep-sea depth level to the bottom using depth level thickness as weights. Subsequently, the GMDST is estimated as the average of all local DST estimates, weighted with the volume of the deep-sea column at that location. In case the surface grid cell areas were part of the model output, the grid cell column volume is defined as the product of horizontal area and vertical thickness. In other cases, a relative grid cell column volume was calculated using the cosine of the grid cell latitude and vertical thickness. For each model simulation, the annual mean local DST was plotted on a (longitude, latitude) grid to visually inspect the results and assess the usability of the data for the intended analysis.

The GMSST and GMSAT estimations resemble that of GMDST, with the difference that vertical averaging was not necessary as the variables are given on a 2-dimensional spatial grid (Table 2). The 12 monthly values were averaged to obtain the annual local means (except for NorESM SST), and the GMSST and GMSAT were derived by area-weighted averaging over all local values. The methods described are also used to estimate the modern values of GMDST, GMSST, and GMSAT using the datasets described in Section 2.2.

Note that GMSAT is defined as the temperature of the air above the land and ocean. A related and commonly used global temperature indicator is the global mean surface temperature (GMST), defined as the mean temperature of the air above the land surface and the temperature of the water at the sea surface. GMST and GMSAT are strongly related, but physically distinct temperature estimates and long-term differences between them are estimated to be at most 10% (Gulev et al., 2021). As the analysis of Hansen et al. (2013) does not specify whether the paleo proxy DST estimates are translated into GMST or

GMSAT, we henceforth make no distinction between GMSAT and GMST and use the abbreviation GMSAT to indicate either estimate.

3.2 Selection of model simulations

To determine whether the model-based temperature estimates can be regarded as equilibrium values, we assessed the degree of energy equilibrium obtained by the model simulations. We based our model simulation selection on a visual inspection of the global annual mean ocean temperature trend, and the global annual mean top-of-atmosphere (TOA) energy imbalance over the last 100 simulation years. Data on ocean temperature time series were not part of the standard DeepMIP database and were requested separately from the model developers. The temperature time series data were available for all EECO simulations except that of INMCM. The underlying ocean cross-section differs per model (Table S3). The global annual TOA energy imbalance per model simulation was calculated as the temporally and spatially weighted average of the difference between net incoming shortwave radiation and outgoing shortwave and longwave radiation (SW↓ - SW↑ - LW↑, Table 2). For the criterion regarding a sufficiently small TOA energy imbalance at the end of the simulation, we followed Lunt et al. (2021) who used a value less than 0.3 W/m^2 or a value similar to that of the PI control run.

We decided to include several model simulations in the regression analyses which have not reached full energy equilibrium yet based on ocean temperature trend. To interpret the values of these simulations, we made the assumption that GMSAT and GMSST have reached equilibrium in all simulations and only the GMDST values of these simulations have not reached equilibrium. The rationale behind this assumption is that the deep-sea takes longer to adjust to the CO$_2$ level than the surface temperatures (Li et al., 2013). In this case, the simulations with a cooling, respectively warming trend have an equilibrium value of GMDST below respectively above the estimated GMDST.

3.3 Assessment of spatial variability DST

The spatial variability of the DST per simulation was analyzed through the weighted distribution of absolute differences between local DST and the GMDST for all (longitude, latitude) locations defined by the surface grid cell, weighted by the volume of the deep-sea below the corresponding surface grid cell. We assessed this distribution by considering several percentiles. Due to the weighting, the interpretation of the xth percentile is that $x\%$ of the total deep-sea volume has an absolute difference between local DST and GMDST less than the percentile value, for x between 0 and 100. Furthermore, we calculated the annual mean DST for the five main oceanic basins: North Atlantic Ocean, South Atlantic Ocean, Southern Ocean, Pacific Ocean, and Indian Ocean (Figure S2). The basin borders are defined such that coastal areas are excluded, in order to obtain stable open ocean basins. The basins are comprised of one or more rectangular (longitude, latitude) boxes following the demarcation in Table S4. This demarcation is applied to all models equally, except for NorESM. This model

11

uses a slightly different paleogeography, and the basin demarcations are adjusted accordingly. The difference between the DST per basin and the GMDST is considered both per model simulation and grouped per oceanic basin for all model simulations together.

3.4 Estimation of temperature relationships

We analyzed the relationships between global temperature indicators by means of linear regression. Three temperature combinations were considered to test the relationships set forth by Hansen et al (2013): GMSST vs GMDST, GMSAT vs GMSST, and GMSAT vs GMDST. For each combination, two linear regressions were performed: one based on only the EECO simulations, and one based on the EECO simulations together with the PI control runs. The linear regression analyses resulted in expression of the first temperature (the dependent variable) as a linear function of the second temperature (the independent variable):

$$T_{\text{dependent}} = \text{slope} \bullet T_{\text{independent}} + \text{intercept}. \quad (1)$$

Estimates of the slope and intercept coefficients were obtained via the ordinary least square method. The fit of the result was assessed by the coefficient of determination R^2. Besides these analyses on global annual means, the same linear regression method is used to analyze the relationship between GMDST and SST in areas of deep-water formation.

3.5 Comparison of model-based and proxy-based GMDST, GMSST, and GMSAT

Using the dataset of 27 marine and 70 terrestrial local temperature proxies (Section 2.3), proxy-based GMSST and GMSAT estimates were obtained by applying the method D_{surf}-2 of Inglis et al. (2020). This method requires two model simulations with different CO_2 levels (low and high CO_2). Assuming a linear relationship between the local and global temperature estimates in the two model simulations, the local proxy-based temperature estimate is scaled to an estimate of global mean temperature. The global mean temperature (GMT, being either GMSST or GMSAT) inferred from a local proxy is defined as:

$$\text{GMT} = \text{GMT}_{\text{low}} + \left(T_{\text{proxy}} - T_{\text{low}} \right) \frac{\text{GMT}_{\text{high}} - \text{GMT}_{\text{low}}}{T_{\text{high}} - T_{\text{low}}} \quad (2)$$

with

- Proxy-based temperature estimate T_{proxy},
- Model-based temperature at the same location for low and high CO_2 (T_{low} and T_{high}),
- Model-based GMT for low and high CO_2 (GMT_{low} and GMT_{high}).

To find the modelled SST at the proxy location, we selected all model grid cells within a certain (longitude, latitude) range of the proxy location. The range

is chosen such that all proxy locations are matched with at least one grid cell. Due to the difference in model resolution (Table 1), this range is model-specific and spans from ($\pm 2°$, $\pm 2°$) for high resolution to ($\pm 5°$, $\pm 5°$) for lower resolution models. The model-based local temperature is then the area-weighted average over the selected grid cells. For GMSST, the transfer function was applied to all 27 local SST proxies in the dataset using the SST estimates of all possible low and high CO_2 simulations of DeepMIP models with multiple simulations. The GMSST estimates for all 27 proxies were averaged to obtain a final estimate of GMSST per combination of low and high CO_2 model simulation. The same method was applied to obtain a proxy-based estimate of GMSAT, using the dataset of 27 marine and 70 terrestrial temperature proxies, the model-based estimates of SAT at the proxy location and GMSAT values. Subsequently, the GMT (either GMSST or GMSAT) estimates for all combination of low and high CO_2 model simulations were first averaged per model, to obtain the mean estimate per DeepMIP model. The average of these values was taken as the final best estimates of GMSST and GMSAT.

The uncertainty of these GMSST and GMSAT estimates was derived following the approach of Farnsworth et al. (2019). The skill of the transfer function was tested by applying the method using model-based instead of proxy-based local temperature estimates. This means that Equation (2) was applied to the temperature estimates from three different model simulations: a low CO_2 simulation, a high CO_2 simulation, and a third distinct simulation taking the place of the proxy-based temperature estimate T_{proxy}. Mirroring the proxy-based GMSST and GMSAT derivations, the transfer function was applied to the modelled local SST estimates on all 27 locations of marine proxies, and to the modelled local SAT estimates on all 97 locations of marine and terrestrial proxies. The average of these 27, respectively 97, estimates was subsequently compared to the actual model-based GMSST, respectively GMSAT, of this third simulation, to assess the offset between the true value and the outcome of the transfer function. This method was applied with all possible combinations of three DeepMIP model simulations with the restriction that the low and high CO_2 simulations are from the same model. The 2.5[th] and 97.5[th] quartiles of the resulting distribution of offsets were used to obtain the 95% confidence interval around the proxy-based GMSST and GMSAT derivations.

For a proxy-based estimate of GMDST, we relied on results available in literature based on recent Δ_{47}-based temperature estimates from the Atlantic (Meckler et al., 2021). Furthermore, we used the estimated GMSAT ranges from Inglis et al. (2020) and Zhu et al. (2019). The 95% confidence interval for the estimate by Zhu et al. (2019) is given, yet Inglis et al. (2020) provide the 66% and 90% confidence intervals. For consistency, we calculated the 95% confidence interval for the estimate by Inglis et al. (2020) by mirroring their approach of Monte Carlo resampling (Section 4.5). Besides these proxy-based temperature estimates, we used a proxy-based best estimate and range for the atmospheric CO_2 concentration during the EECO for the model-proxy comparison (Anagnostou et al., 2020; Rae et al., 2021).

3.6 Sensitivity analysis

As part of the analysis, we made choices regarding the definition of the deep-sea, inclusion of oceanic basins and model simulations included in the analysis. Specifically, we defined the deep-sea as the part of the ocean ranging from a depth of 2,000 m to the ocean floor (Section 3.1). Furthermore, we decided to exclude the Arctic Ocean from the calculations of GMDST and GMSST (Section 4.1) and we decided to include several simulations that did not reach full equilibrium (CESM, IPSL, and NorESM $4xCO_2$; Section 4.2). In the sensitivity analysis, we assessed the sensitivity of the GMDST value to the deep-sea definition, and we repeated the linear regression analysis for different deep-sea definitions, for the ocean including the Arctic, and only for the model simulations that reached full energy equilibrium. We assessed the sensitivity of the linear regression results from the main analysis by comparing the regression slopes of the main analysis with the slopes of the sensitivity analysis.

4 Results

4.1 Estimates of GMDST, GMSST, and GMSAT

An overview of the GMDST, GMSST, and GMSAT for the EECO and PI simulations is given in Table 3, and visually depicted in Figure 2. After a visual inspection of the analysis results, we made two changes to the data underlying the analysis. First, there are small outlier sections in some EECO model simulations, where the DST values were several °C higher or lower than those of the surrounding area. These sections span a couple of grid cells in the Arctic gateway east of Greenland for COSMOS, HadCM High Resolution, INMCM, and MIROC, and between the Australian and Antarctic continents for COSMOS and IPSL. These outliers were manually removed from the data. Secondly, we chose to exclude the Arctic Ocean from the calculations of GMDST and GMSST. Inspection of the model ocean bathymetry showed that the Arctic was poorly connected with the rest of the ocean during EECO with a maximum gateway depth in the CESM simulations of about 600 m (Figure 1(a)), limiting deep-water exchange. The Arctic was removed from the data by excluding the surface grid cells with latitudes above 65 °N. To assess the impact of this exclusion, we performed a sensitivity analysis based on GMDST and GMSST estimates including the Arctic (Section 4.6).

As expected, the global mean temperatures increase with increasing CO_2 level. Furthermore, the temperatures in the $1xCO_2$ runs are higher than those of the PI runs for all models with a $1xCO_2$ simulation. This difference is due to non-CO_2-related effects such as differences in continental configuration, vegetation, and presence of ice sheets (Lunt et al., 2021). The average difference between the $1xCO_2$ run and the PI control run is 2.1 °C for GMDST, 3.5 °C for GMSST, and 3.8 °C for GMSAT. Hence, the response to non-CO_2 climatic factors seems stronger at the surface than in the deep-sea. However, the variation between models for GMDST $1xCO_2$ run and PI difference is considerable, from as low as 0.5 °C for COSMOS and MIROC to almost 5°C for CESM. This indicates

14

that the models vary in their sensitivity of GMDST to the non-CO_2 effects. Note however that the models vary in run time (Table 1) and degree of energy equilibrium for the 1xCO_2 simulations (Table 3).
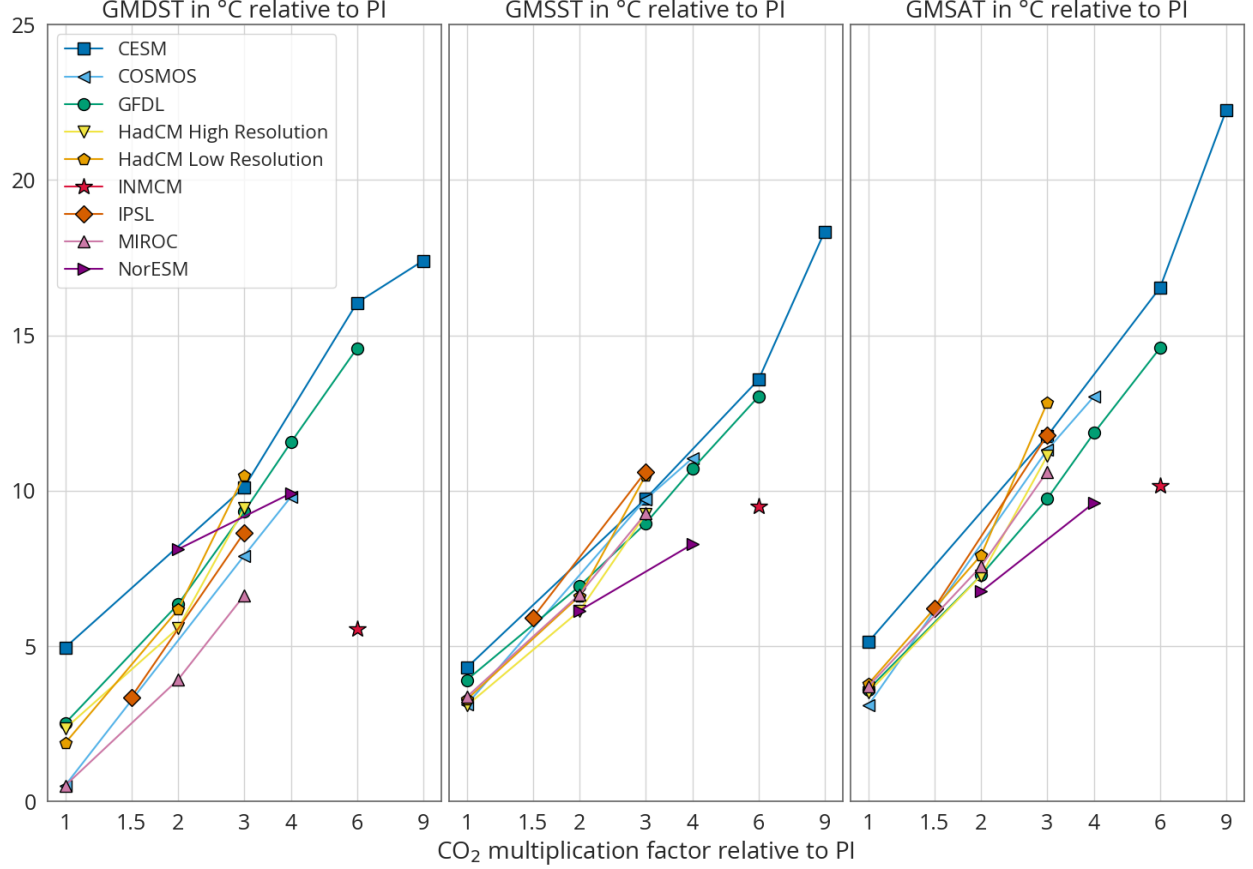

Figure 2. GMDST (left), GMSST (middle), and GMSAT (right) relative to the PI value as a function of CO_2 multiplication factor (horizontal) for the DeepMIP EECO model simulations. The global mean temperature values of each model are depicted with a different color and symbol and the values of different simulations with the same model are connected with a line. The CO_2 multiplication factors on the horizontal axis are plotted on a logarithmic scale.

Table 3. GMDST, GMSST, GMSAT, TOA energy imbalance, and ocean temperature trend per simulation. For the EECO simulations, absolute TOA energy imbalance values of at least 0.30 W/m^2 are in bold, unless the value is similar to that of the PI control run. Ocean temperature trends of at least 0.5 °C/1000 yrs in absolute value are also in bold.

Model	Simulation	GMDST in °C	GMSST in °C	GMSAT in °C	TOA energy imbalance in W/m²	Ocean temperature trend in °C/1000 yrs
CESM	PI				+0.01	
	1xCO$_2$					**-0.66**
	3xCO$_2$				**-0.30**	**-0.89**
	6xCO$_2$				**+0.37**	**+0.91**
	9xCO$_2$				**+0.68**	**+1.72**
COSMOS	PI				+1.78	
	1xCO$_2$				+1.95	
	3xCO$_2$				+1.82	+0.14
	4xCO$_2$				+1.98	+0.15
GFDL	PI				+0.30	
	1xCO$_2$				+0.08	
	2xCO$_2$					
	3xCO$_2$					
	4xCO$_2$					
	6xCO$_2$					
HadCM High Resolution	PI					
	1xCO$_2$				+0.00	+0.07
	2xCO$_2$					
	3xCO$_2$					
HadCM Low Resolution	PI					
	1xCO$_2$					+0.20
	2xCO$_2$					+0.11
	3xCO$_2$				+0.04	+0.31
INMCM	PI				+4.36	
	6xCO$_2$				**+2.86**	
IPSL	PI				+0.10	
	1.5xCO$_2$				**+0.61**	
	3xCO$_2$				**+0.79**	
MIROC	PI				+0.96	
	1xCO$_2$				+0.77	+0.00
	2xCO$_2$				+0.90	+0.00

Model	Simulation	GMDST in °C	GMSST in °C	GMSAT in °C	TOA energy imbalance in W/m²	Ocean temperature trend in °C/1000 yrs
NorESM	3xCO$_2$				+0.97	
	PI				+0.03	
	2xCO$_2$				+0.06	
	4xCO$_2$				+0.27	**+0.59**

4.2 Model simulation selection

We assessed both the global mean TOA energy imbalance and the global mean ocean temperature trend at the end of the simulation. The TOA energy imbalance primarily reflects the energy equilibrium at the surface, while the ocean temperature trend determines the degree of energy equilibrium in the deep ocean, Lunt et al. (2021) set the criterion for TOA energy imbalance at less than 0.3 W/m^2 or similar to that of the PI control run. This criterion does not hold for CESM 3xCO$_2$, 6xCO$_2$ and 9xCO$_2$, INMCM and both runs of IPSL (Table 3). Note that COSMOS and MIROC have a TOA energy imbalance above 0.3 W/m^2, which is however similar in value to that of the PI control run. The comparison between EECO and PI value is necessary for models that do not reach a low TOA energy imbalance due to non-conservation of energy. This is for example the case for COSMOS (Stevens et al., 2013). Another reason for a high TOA energy imbalance can be that the calculation is made at the top of the model atmosphere instead of the full atmosphere, which is the case for INMCM (Lunt et al., 2021).

The ocean temperature trends of CESM 6xCO$_2$ and 9xCO$_2$ and NorESM 4xCO$_2$ are above 0.5 °C/ 1000 years at the end of the simulations (Table 3). Hence, the deep ocean is still taking up heat at the end of these simulations, and the equilibrium GMDST value is expected to be higher than the end-of-simulation GMDST. On the other hand, the runs CESM 1xCO$_2$ and 3xCO$_2$ show a considerable cooling trend of more than 0.5 °C/ 1000 years. The other model simulations show a more modest ocean temperature trend, indicating that the end-of-simulation GMDST is close to the equilibrium GMDST. Note that the ocean temperature trends of COSMOS and MIROC are close to 0. This indicates that these simulations are close to equilibrium, and the relatively high TOA imbalance value is related to non-conservation of energy. Combining these findings, we conclude that:

- The simulations of COSMOS, GFDL, HadCM High and Low Resolution, MIROC, and NorESM 2xCO$_2$ are close to equilibrium,

- The simulations of CESM, IPSL, and NorESM 4xCO_2 have not reached full equilibrium yet.

- There is insufficient information to correctly interpret the degree of equilibrium of INMCM.

Based on this assessment, we decided to include all simulations except INMCM in the analysis with the realization that caution is needed to correctly interpret the results regarding CESM, IPSL, and NorESM 4xCO_2. For the interpretation of these simulations, we assumed that only the GMDST values have not reached equilibrium. The results of INMCM are not used in the analysis but are included in the figures and tables, for reference and completeness.

4.3 Spatial variability in DST

To gain insight into the spatial variability of the DST in the model simulations of the EECO climate, the results of the annual mean DST in the different CO_2 model simulations are plotted on a (longitude, latitude) grid using a Robinson projection (Figure S3). Comparing the different simulations from the same model, we see that the spatial temperature distribution of relatively warm and cold regions stays roughly the same with increasing CO_2 level. Furthermore, the results show that the spatial variability for DST is limited to a few °C in the model simulations. There is a warm tendency in the parts of the deep-sea that are relatively shallow, such as the Mid-Atlantic Ridge and coastal zones around North America and Africa. This can be clearly seen in the simulations of CESM, HadCM and NorESM. Several models, such as COSMOS, GFDL, HadCM and IPSL, show a relatively large temperature difference between the deep-sea south and east of the Australian continent. Except for these warm regions south of Australia, the Southern Ocean is the coldest in the simulations.

To further analyze the spatial variability of DST, Figure 3 presents boxplots of the absolute difference between the local DST and the GMDST for all the simulations weighted by local volume of the deep-sea. The same plot for only the locations that belong to the five main open oceanic basins (Figure S2) is given in Figure S4. The COSMOS model has the most homogeneous DST, with 98% of the deep-sea volume differing less than 0.5 °C from the mean. The models INMCM, MIROC and NorESM show most spatial variability in DST. Regarding NorESM, a possible cause for this spatial variability is the weak meridional overturning circulation displayed in these simulations (Zhang et al., 2022). The other models show a DST anomaly of no more than 2 °C when excluding the outliers beyond the 99th percentile. For all model simulations except NorESM 2xCO_2 (and INMCM), 50% of the deep-sea volume differs less than 0.4 °C from the GMDST, 75% less than 0.7 °C, and 90% less than 1.5 °C. When only considering the five main open oceanic basins (Figure S4), it holds that 50% of the deep-sea volume differs less than 0.4 °C from the GMDST, 75% less than 0.6 °C, and 90% less than 0.8 °C, for all model simulations except NorESM 2xCO_2 (and INMCM). This indicates that the open oceanic basins are more homogeneous in DST than the parts of the deep-sea that lie closer

to the continents. Model resolution can also impact the model results in these relatively shallow parts of the ocean near the continents, as coastal regions are more difficult to resolve on a relatively coarse ocean model grid.

The difference between the DST per oceanic basin and the GMDST is depicted in Figure 4 grouped per oceanic basin for all models except INMCM, and in Figure S5 grouped per model. The plots show that the mean DST of the Pacific Ocean agree best with the GMDST, partly because of the relatively large area covered by the Pacific. In most simulations, the Southern Ocean is colder, and the North-Atlantic Ocean is warmer than the global average. The results for the Indian Ocean and the South-Atlantic Ocean show more variability with simulation and model. For 84% of the 125 combinations of 25 model simulations (excluding INMCM) and 5 basins, the absolute difference between basin and global mean DST is less than 0.5 °C, and for 95% of the combinations it is less than 1 °C. From this analysis we conclude that the spatial variability for DST in basins is low. All basins are more or less representative of the global mean, with a cold tendency in the Southern Ocean and warm tendency North-Atlantic.
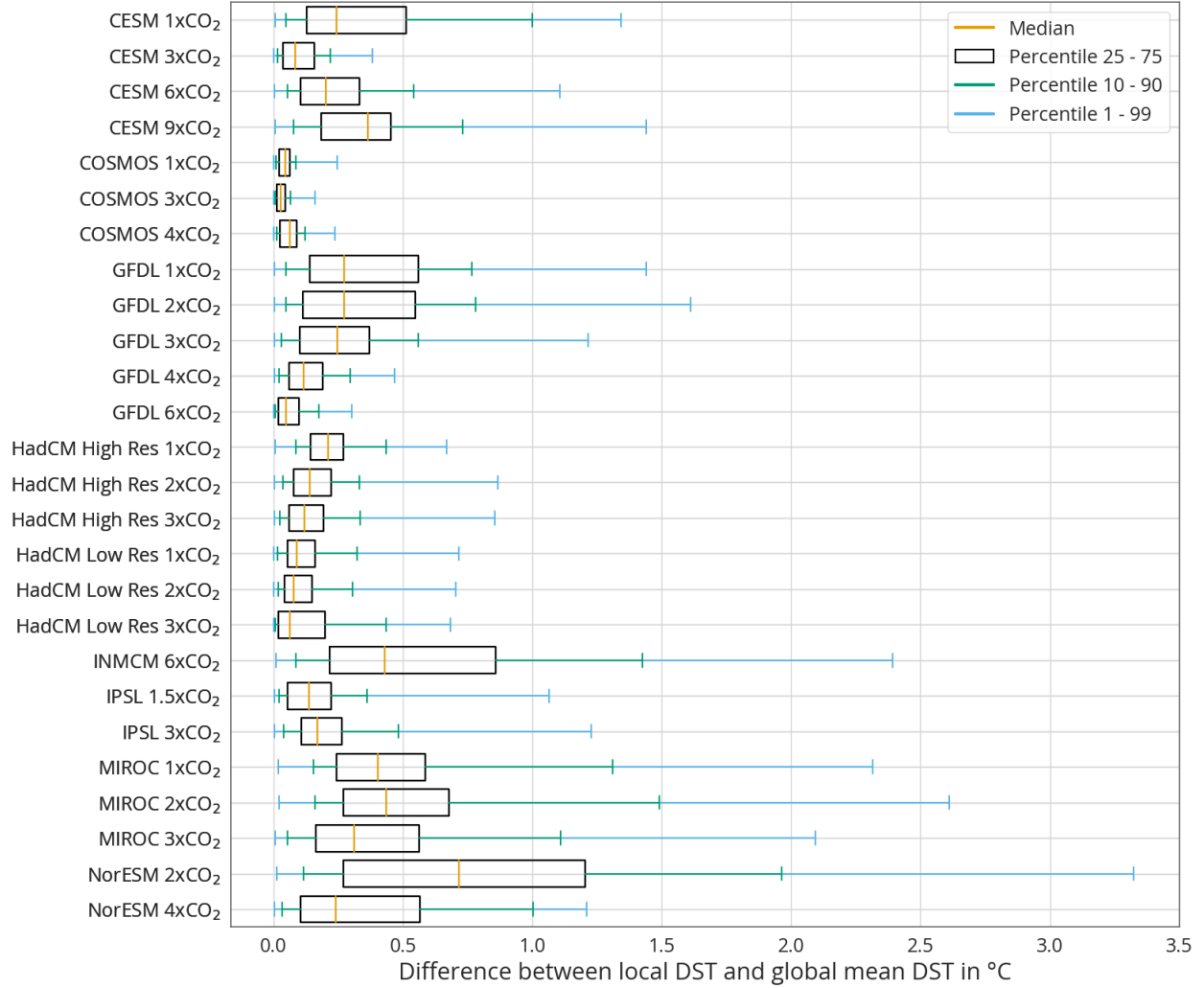
Figure 3. Local DST anomaly in absolute value from GMDST in °C for all model simulations. The boxplots show the distribution of the absolute difference between the local DST and the GMDST for all the ocean surface grid cells weighted by the volume of the deep-sea below that grid cell. The orange vertical line indicates the median (50th percentile), the black box ranges from the 25th to the 75th percentile, the green vertical lines extending from the box range from the 10th to the 90th percentile, and the blue lines from the 1st to the 99th percentile.
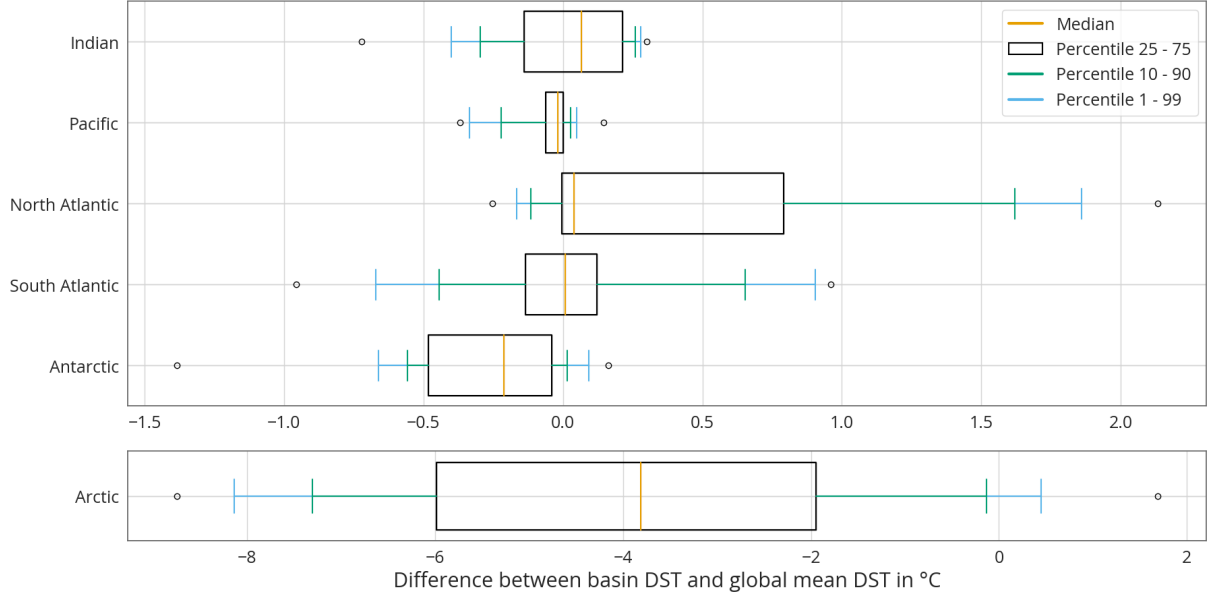
Figure 4. Difference between basin mean and global mean DST in °C for all the DeepMIP EECO model simulations except INMCM grouped per basin. The Arctic Ocean (defined as all latitudes north of 65 °N) is plotted for reference with a different range for the horizontal axis. Color codes of the boxplot and vertical lines are the same as for Figure 3. The small open circles indicate the outliers beyond the 1st and 99th percentile.

4.4 Temperature relationships

4.4.1 Relationship between GMDST, GMSST, and GMSAT

The linear regression results are presented in Table 4, and visually depicted in Figure 5. All regressions show a good fit with the data, based on the R^2 value of at least 0.95. The relationship between GMDST and GMSAT is of special interest, as the GMSAT evolution during the Cenozoic presented in IPCC AR6 is based on the translation of paleo-proxies of DST into GMSAT estimates (Gulev et al., 2021). The slope of the linear regression in the EECO only case (0.99) implies that changes in GMDST relate almost 1-on-1 to changes in GMSAT. This means that the slopes of the linear regressions between GMDST and GMSST (1/1.18) and between GMSST and GMSAT (1.17) cancel out each other almost completely. This is not the case for the combination of EECO and PI simulations, in which case the slope between GMDST and GMSAT is 1.09.
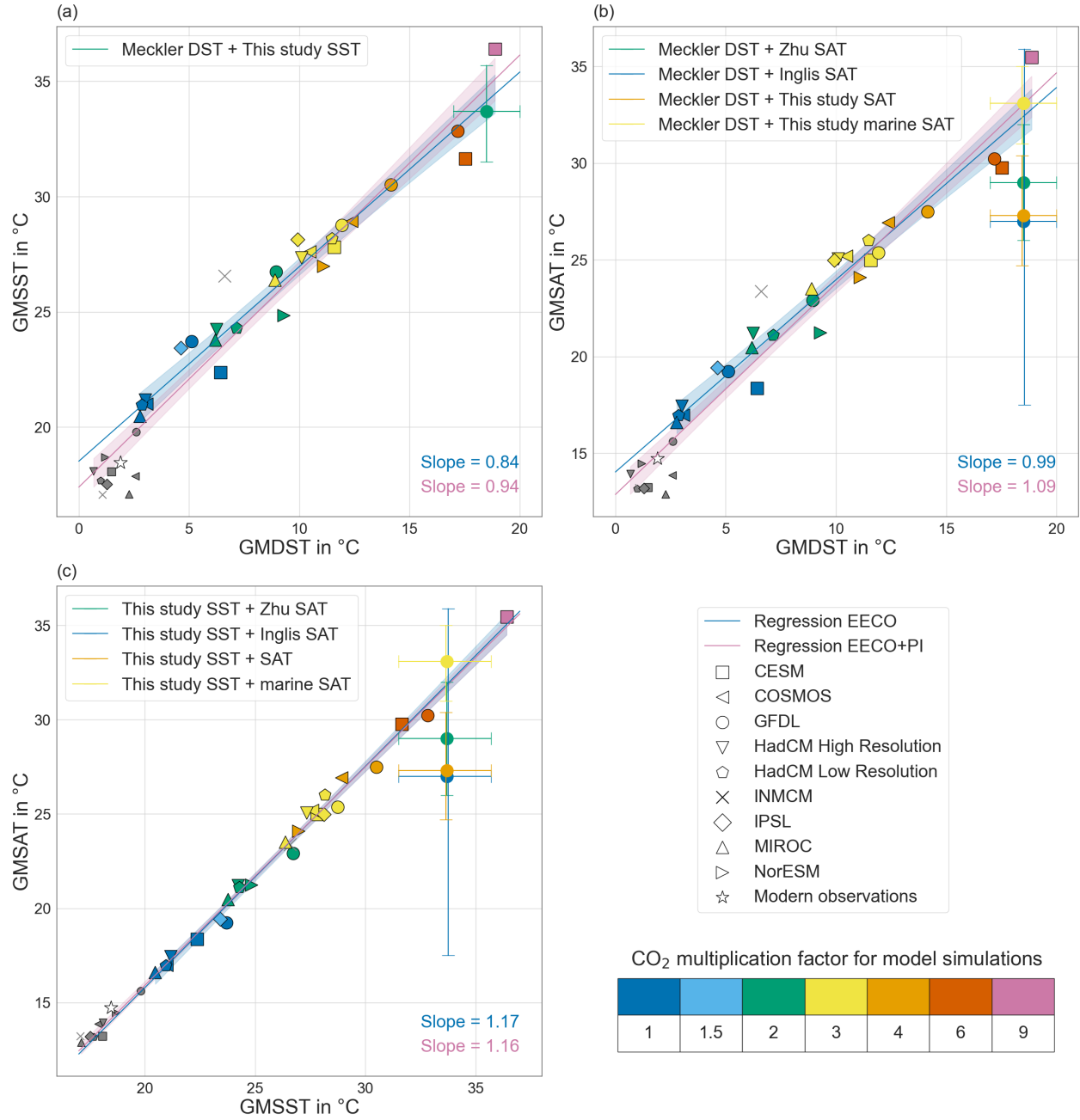
21

Figure 5. Relationship between (a) GMDST and GMSST, (b) GMDST and GMSAT, and (c) GMSST and GMSAT. The results of the EECO simulations except for INMCM are depicted with large symbols indicating the model, and colors indicating the CO$_2$ multiplication factor. The results of the PI run are

depicted with small grey symbols, and the results of INMCM are depicted with grey crosses. Reference values for modern temperatures are depicted with black hexagons (Table S1). The regression results based on all models except IN-MCM are depicted in blue (EECO) and pink (EECO+ PI), with 95% confidence bands in shading. The colored dots mark combinations of proxy-based GMDST, GMSST, and GMSAT estimates, and the vertical and horizontal lines extending from the dots indicate the corresponding 95% confidence intervals (Section 4.5).

We included model simulations in the regressions which have not reached full energy equilibrium yet, and we assumed that only the GMDST values of these simulations have not reached equilibrium. In the plots with GMDST as independent variable, this means that the equilibrium GMDST of cooling simulations lie to the left of their current position, and those of warming simulations to the right. For CESM $1xCO_2$, $3xCO_2$ and $9x$ CO_2, this means that the equilibrium values move towards the regression line. Contrarily, CESM $6xCO_2$, both IPSL simulation and NorESM $4x$ CO_2 move away from the regression line. Hence, there is no uniform relationship between the sign of temperature trend and the position relative to the regression line for the non-equilibrium simulations. We discuss the effect of the non-equilibrium simulations on the regression results in more detail as part of the sensitivity analysis (Section 4.6).

Table 4. Regression results between GMDST, GMSST, and GMSAT for the relationships presented in Figure 5. The standard error (SE) of the slope is given in parentheses.

Independent variable	Dependent variable	Regression EECO	Regression EECO + PI		
		Slope (SE)	Intercept	R^2	Slope (SI
GMDST	GMSST	0.84 (0.04)	18.52	0.96	0.94 (0.04)
GMSST	GMSAT	1.17 (0.03)	-7.69	0.99	1.16 (0.02)
GMDST	GMSAT	0.99 (0.05)	14.04	0.95	1.09 (0.04)

4.4.2 Temperature relationship for the Antarctic winter area

As stated in Section 1, Hansen et al. (2013) assume that GMDST is essentially determined by the SST at areas of deep-water formation (DWF). Hence, the relationship in the EECO simulations between GMDST and SST at these sites is of special interest. In the DeepMIP simulations, the Antarctic region is the predominant area of deep-water formation, and DWF is strongest in the Antarctic winter (June, July, and August) (Zhang et al., 2022). Therefore, we analyzed the relationship between GMDST and Antarctic winter SST. The NorESM is excluded from the analysis of the Antarctic winter SST, as only annual mean SST estimates are available for NorESM. We defined the Antarctic area of the Southern Ocean as the part consisting of surface grid cells with latitudes south of 60 °S. Note that this simplified definition does not include all DWF areas, as the GFDL model simulations also show DWF in the northern Pacific (Zhang et al., 2022).

The linear regression results are presented in Figure 6. The two regressions show a good fit with the data, based on the R^2 values of 0.93 and 0.94. The slope of the regression based on the combination of EECO and PI simulations is larger than that of the EECO regression. This means that the Antarctic winter SST for the PI simulations is colder than would be expected from the EECO-regression. The difference between Antarctic winter SST in the PI and $1xCO_2$ runs is substantiated by a Student's t-test hypothesis, rejecting the hypothesis that the Antarctic winter SST values for the PI runs and the $1xCO_2$ simulations are drawn from the same population (p-value = 0.0003). The slope of the EECO-regression is 0.97, indicating that there is indeed a strong relationship between Antarctic winter SST and GMDST, yet Antarctic winter SST is a little less sensitive to changes in CO_2 than GMDST.

Fi
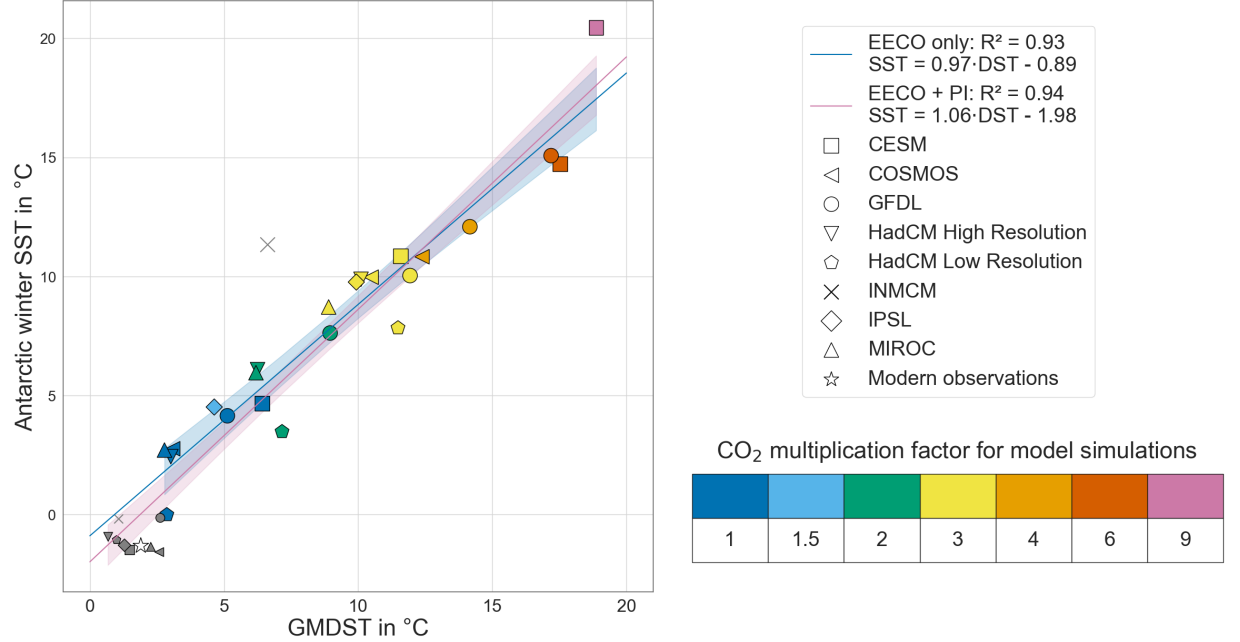
6. Relationship between GMDST and Antarctic winter SST. Colors and symbols are the same as in Figure 5. Standard error of EECO only slope is 0.06, and that of the EECO+PI slope is 0.05.

4.5 Comparison of model-based and proxy-based GMDST, GMSST, and GMSAT

Figure 5 includes paleo-proxy based estimates of GMDST, GMSST, and GMSAT. The paleo-proxy range for the GMDST during EECO is shown to be 17-20 °C based on recent Δ_{47} analysis (Meckler et al., 2021). To obtain estimates of GMSST and GMSAT, we applied the transfer function of Equation (2) to the set of 27, respectively 97, paleo-proxies using the DeepMIP model simulations (Tables S5 and S6). The 95% confidence intervals (CI) around these GMSST

and GMSAT estimates were determined from the distribution of offsets between the true value and the value estimated by the transfer function applied to the model-based local temperature estimates of the DeepMIP models (Figure S6). Note that the estimates of COSMOS in Tables S5 and S6 deviate from those of the other models and have a high standard deviation for both the GMSST and GMSAT estimates. Leaving out the COSMOS results from the averaging, we obtain mean proxy-based estimates of 33.7 °C (95% CI: 31.5 – 35.7) for GMSST and 27.3 °C (95% CI: 24.7 – 30.4) for GMSAT. Additionally, we derived an estimate of GMSAT based on solely the 27 marine temperature proxies (Table S7). Again, excluding the COSMOS estimates, this results in a GMSAT of 33.1 °C (95% CI: 31.0 – 35.0), considerably higher than when the terrestrial proxies are also taken into account.

Furthermore, Inglis et al. (2020) and Zhu et al. (2019) provide proxy-based estimates of GMSAT. Inglis et al. (2020) derive a best estimate of 27.0 °C with 66% CI of 23.2 – 29.6, and Zhu et al. (2019) arrive at an estimate of 29 $\pm$ 3 °C (95% CI). Inglis et al. (2020) do not include a 95% CI in their documentation. For consistency with the other estimates, we derived a 95% confidence interval for the best estimate of Inglis et al. (2020) by reproducing their approach of Monte Carlo resampling with full propagation of errors on the intermediate results provided in their Table 3. The resulting 95% CI spans 17.5 – 35.9 °C.

The proxy-based estimate of atmospheric CO_2 during EECO range is 1,150 – 2,000 ppm with a best estimate of 1,500 ppm (Anagnostou et al., 2020; Rae et al., 2021). This translates to a range of 4.1 and 7.1 times the preindustrial CO_2 level, with a best estimate of 5.4. Comparing the model-based and proxy-based temperature estimates, we see that the 6xCO_2 simulations of GFDL and CESM correspond best with the proxy reconstructions (Figure 5). Both simulations lie within the 95% CI of GMDST, GMSST, and the GMSAT estimates of this study, Zhu et al. (2019), and Inglis et al. (2020). This CO_2 level of 1,680 ppm corresponds well with the proxy-based range of CO_2 of 1,150 – 2,000 ppm. Hence, there is agreement between models and proxies concerning the relationship between GMDST, GMSST, GMSAT, and CO_2 level.

1. Sensitivity analysis

Typically, the term deep-sea refers to the ocean below the thermocline at a depth of 1,500-2,000 m. In our research, we define the deep-sea as the part of the ocean below 2,000 m depth. This demarcation corresponds with the study of deep ocean warming by Desbruyères et al. (2016) and the assessment of ocean heat uptake in IPCC AR6 in which the ocean below 2,000 m is considered separately from the upper layers (Gulev et al., 2021). To understand the sensitivity of our results to the chosen 2,000 m demarcation, the difference between the GMDST starting at 2,000 m and GMDST starting at depth levels between 1,000 and 4,000 m is analyzed (Figure S7). On average, the GMDST increases when starting at a shallower depth level. This means that the ocean temperature decreases with depth level. For most model simulations, the difference between the GMDST estimate used in the analyses and the other GMDST estimates is less than 0.6°C.

The model that shows the most variability is INMCM. Other model simulations with a relatively high sensitivity regarding deep-sea definition are the CESM $9xCO_2$ and the NorESM simulations. A possible explanation is that the ocean has not reached thermal equilibrium yet in the model simulation. In such a case, the temperature of the (deep-)ocean is still adjusting to the prescribed CO_2 scenario. The model simulations CESM $9xCO_2$ and NorESM $4xCO_2$ show a considerable warming trend for the full ocean at the end of the simulation (Table 3), indicating that the ocean is indeed still taking up considerable heat. The NorESM $2xCO_2$ simulation does not have such a warming trend for the full ocean (Table 3), yet the different ocean layers could still be exchanging energy. The relatively large difference between GMDST starting at 4,000 m and 1,000 m for this model simulation could indicate that the deep ocean is still warming.

We assessed the sensitivity of the linear regression results from the main analysis by performing a linear regression for different definitions of the deep-sea, only the model simulations that have reached full energy equilibrium and for GMDST and GMSST estimates including the Arctic. We duplicated the linear regression for definitions of the deep-sea starting at 1,500 m, 2,500 m, and 3,000 m (Table 5). The slope and fit of the linear regression results are comparable for the different deep-sea definitions. Hence, the relationships between changes in GMDST, GMSST and GMSAT are little affected by the deep-sea definition. The intercepts show a slightly increasing trend with the starting level of the deep-sea. This agrees with the decreasing value of GMDST with starting depth (Figure S7): the difference between GMSST/GMSAT and GMDST increases when the deep-sea threshold is deeper. The intercept of the linear regression captures this constant difference between GMSST and GMDST.

Comparing the regression results for only the model simulations in equilibrium (Table 6) with those of the regressions based on all simulations (Table 4), we see that the slope decreases for both GMSST versus GMSAT, and GMDST versus GMSAT, yet remains unchanged for GMDST versus GMSST. As a result, the relationship between changes in GMDST and in GMSAT is not completely 1-to-1 in the EECO only case. Instead, the GMSAT is about 4% less sensitive to CO_2 changes than the GMDST (slope of 0.96).

The differences between the linear regressions based on data including the Arctic (Table 7) and those excluding the Arctic region (Table 4) are small. We observe an approximate 1-to-1 relationship between GMDST and GMSAT in regressions based on EECO data when including the Arctic Ocean. In the regression based on the combination of EECO and PI simulations, the GMSAT responds about 9% stronger than GMDST to atmospheric CO_2 changes (slope of 1.09). These results are very similar to the results without the Arctic (Table 4). From this we conclude that the linear regression results are only weakly sensitive to the inclusion or exclusion of the Arctic region in the analysis.

Table 5. Regression results between GMDST, GMSST, and GMSAT for different definitions of deep-sea. The standard error (SE) of the slope is given in parentheses.

26

Independent variable	Dependent variable	Regression EECO	Regression EECO + PI		
		Slope (SE)	**Intercept**	**R^2**	**Sl**
Deep-sea starting at 1,500 m					
GMDST	GMSST	0.85 (0.04)	18.41	0.96	0.9
GMDST	GMSAT	1.00 (0.05)	13.89	0.95	1.1
Deep-sea starting at 2,500 m					
GMDST	GMSST	0.85 (0.04)	18.59	0.96	0.9
GMDST	GMSAT	0.99 (0.05)	14.13	0.95	1.0
Deep-sea starting at 3,000 m					
GMDST	GMSST	0.85 (0.04)	18.63	0.96	0.9
GMDST	GMSAT	1.00 (0.05)	14.17	0.95	1.0

Table 6. Regression results between GMDST, GMSST, and GMSAT based on only the model simulations in equilibrium. The standard error (SE) of the slope is given in parentheses.

Independent variable	Dependent variable	Regression EECO	Regression EECO + PI		
		Slope (SE)	**Intercept**	**R^2**	**Slope (SE)**
GMDST	GMSST	0.84 (0.03)	18.62	0.98	0.94 (0.04)
GMSST	GMSAT	1.14 (0.04)	-6.82	0.98	1.14 (0.02)
GMDST	GMSAT	0.96 (0.04)	14.40	0.97	1.07 (0.05)

Table 7. Regression results between GMDST, GMSST, and GMSAT including the Arctic region. The standard error (SE) of the slope is given in parentheses.

Independent variable	Dependent variable	Regression EECO	Regression EECO + PI		
		Slope (SE)	**Intercept**	**R^2**	**Slope (SE)**
GMDST	GMSST	0.86 (0.04)	17.92	0.96	0.92 (0.03)
GMSST	GMSAT	1.16 (0.02)	-6.78	0.99	1.19 (0.01)
GMDST	GMSAT	1.00 (0.05)	14.04	0.95	1.09 (0.04)

5 Discussion

The current understanding of temperatures at the Earth's surface during the Cenozoic era as presented in IPCC AR6 relies on paleo-proxies of DST combined with assumptions regarding the relationship between DST and GMSAT, most notably through the work of Hansen et al. (2013) and Westerhold et al. (2020). Our findings can be used to test whether two important underlying assumptions hold during the EECO:

1. A local DST estimate is representative for GMDST.

2. GMDST and GMSAT are equally sensitive to changes in atmospheric CO_2 concentrations.

We discuss assumption 1 through our model-based research results regarding the spatial variability of DST, and assumption 2 through our results about the relationship between GMDST, GMSST, and GMSAT.

5.1 Using local DST to infer GMDST

A characteristic feature of the current deep-sea is its spatial temperature homogeneity. Essentially this means that global DST is determined by the surface temperature at the location of deep-water formation, and the DST change during the subsequent circulation of the deep part of the full global ocean is limited. Insight into the spatial variability of DST during paleo climates is essential, as spatial homogeneity is an important prerequisite for using local paleo proxies of DST as indicator of GMDST. In the DeepMIP EECO simulations, we indeed observe limited spatial variability in DST (Figures 3 and S4). For all but one model simulation, 90% of the deep-sea volume differs less than 0.8 °C from the GMDST in the open oceanic basins. This limited spatial variability implies that local open ocean palaeoceanographic proxies of deep-sea temperature can be regarded as representative of the GMDST. Proxies from locations closer to the continents may be subject to more spatial temperature variability. The Δ_{47}-estimate of GMDST we derived from Meckler et al. (2022) is based on fossils from open ocean basins with paleo-depths of 1,500 m and 3,050 m. Note that our analysis uses a deep-sea definition starting at a depth of 2,000 m, while paleo-proxies of DST are taken from different paleo-depths. The sensitivity analysis shows that the dependence of GMDST value on the starting depth of the deep-sea is limited: the absolute difference between a GMDST value starting at 1,500 or 3,000 m depth and that starting at 2,000 m is no more than 0.2 °C in most model simulations (Figure S7). This indicates that the impact of the different paleo-depths of the proxies on the DST estimate is limited.

Continental configuration and bathymetry can be the cause of spatial variability in DST. There is a warm tendency in the relatively shallow parts of the ocean, such as the Mid-Atlantic Ridge and coastal zones around North America and Africa. Furthermore, several models show a relatively large temperature difference between the deep-sea south and east of the Australian continent, which is related to the narrow Tasman Seaway between Antarctica and Australia, preventing ocean circulation. This aligns with the analysis of Sijp et al. (2011): in their Eocene model simulations with a closed Tasman Seaway and open Drake Passage there are two separate subpolar gyres, and these gyres are replaced by a zonally oriented circumpolar current in response to a deepening of the Tasman Seaway. The model simulations of Sauermilch et al. (2021) also show that transport through the shallow Tasman Gateway during the Eocene is limited. Furthermore, Baatsen et al. (2020) show that there is a difference in deep-water age on both sides of the Tasman Seaway in simulations of the Late Eocene climate, whereas the Antarctic deep-water during the preindustrial has a more uniform age. Their Late Eocene simulation also shows a limited deep-water

28

circulation in the North-Atlantic due to the continental configuration and the lack of northern DWF.

Looking at the DST per basin, we note that compared to the GMDST, the Southern Ocean deep-sea is relatively cold and the North-Atlantic deep-sea relatively warm (Figure 4). These temperature variations can have several causes. Regarding the Southern Ocean, there may be interannual variability in the Antarctic winter SST, implying that the source of deep-water varies in temperature. The full circulation of deep ocean water takes millennia, so these temperature differences slowly spread throughout the oceanic basins. Another possible factor for inter-basin temperature variations can be diffusion of heat from the upper layers to the deep ocean. This would mean that the GMDST is not fully determined by the Antarctic SST, but also by the SST of the other oceanic basins. Particularly in basins that are further away from the DWF area there can possibly be mixing of the deep-water with the water masses above that are warmed from diffused heat. This could be the case for the North-Atlantic since there is no DWF in this area in the DeepMIP EECO simulations. An interesting topic of further research would be to analyze whether heat diffusion significantly contributes to DST in warm climates such as the EECO, and if the deep ocean takes longer to equilibrate as a consequence.

In this regard, we note that several model simulations still show a cooling or warming trend in deep or full ocean temperature at the end of the simulation, predominantly the simulations of CESM, IPSL, and NorESM $4xCO_2$ have not reached full equilibrium yet. The strength of the overturning circulation in the $3xCO_2$ simulations of 18 Sv or more as estimated by Zhang et al. (2022) suggests that a full circulation of the deep-ocean water can be expected to take less than 2,400 years in case of a sufficiently deep global overturning cell based on an ocean volume of $1.335 \cdot 10^{18}$ m^3. If the DST is fully determined by the SST at DWF areas, an equilibrium can be expected after a full overturning circulation. Hence, the presence of a cooling or warming trend in ocean temperature after multiple millennia can indicate that diffusion of heat from the upper layers to the deep ocean plays a role in determining DST as well. This aligns with the results of Li et al. (2013). In their model simulation based on modern continental configuration and bathymetry, the GMSST has reached equilibrium after about 1,200 years and the full ocean after 4,600 years, displaying a near-uniform warming with water depth. Hence, in this experiment it took the deep ocean 3,400 years to reach equilibrium after the sea-surface had fully responded to a climate perturbation.

Looking at paleo-proxy based research into the inter-basin temperature variability during the EECO, Cramer et al. (2009) found that ^{18}O isotopic differences between the North-Atlantic, South-Atlantic, Pacific, and Southern Ocean were at most 0.5‰ in the Early Eocene ocean. The ^{18}O are most negative for the North-Atlantic Ocean, aligning with the relatively warm deep ocean in the DeepMIP model simulations. In an ice-free world, we can approximate the relationship between temperature and ^{18}O by assuming an approximate 4 °C

temperature change per 1‰ change in ^{18}O (Hansen et al., 2013; Kim & O'Neil, 1997). Hence, the inter-basin difference of 0.5‰ corresponds to a deep-sea temperature variability of at most 2 °C. This proxy-based estimate is higher than our estimate of the temperature variability of the open ocean basins (Figure S4) but is in alignment with the model-based finding that 90% of the full deep ocean has a temperature difference of less than 1.5 °C (Figure 3).

5.2 The relationship between GMDST and GMSAT

Our linear regression results align with the reasoning set forth by Hansen et al. (2013) regarding the sensitivities of GMDST, GMSST, and GMSAT to a change in atmospheric CO_2. There is an almost 1-to-1 relationship between GMDST and GMSAT (linear regression slope = 0.99 with standard error 0.05), and also there is a strong relationship between Antarctic winter SST and GMDST (slope = 0.97 with standard error 0.06). The 1-to-1 relationship between GMDST and GMSAT is not sensitive to the definition of deep-sea starting depth (Table 5), yet is less strong when considering only the model simulations that have reached full equilibrium (slope 0.96; Table 6) and when using the regression results based on the EECO simulations and the PI control runs together (slope 1.09; Table 4). This means that, based on both EECO and PI model runs, the GMSAT is 9% more sensitive to a CO_2 change than GMDST. Furthermore, the Antarctic winter SST for the PI simulations is colder than would be expected from the EECO-regression. This can possibly be explained by albedo effects from the ice sheet on Antarctica a in the preindustrial, causing an amplification of surface temperature changes near the southern pole in the PI control runs. Several other mechanisms could cause a relatively cold Antarctic winter SST in the PI compared to the $1xCO_2$ EECO, such as a shift in the Antarctic coastline or sinking regions, and changes in the position and strength of the Antarctic Circumpolar Current.

Our analysis indicates that the assumptions of Hansen et al. (2013) are valid for the full set of model simulations of the EECO climate, but that this result cannot immediately be translated to validate the assumption for other climate states, such as the preindustrial one. This corresponds well with the research of Valdes et al. (2021) that covers the whole Phanerozoic era. Analyzing data from this 540-million-year long period, they find a relatively strong linear relationship between GMDST and GMSAT yet with variable slope. The overall slope for the whole Phanerozoic is 0.64 (R^2 = 0.74), which increases to 0.67 (R^2 = 0.90) when only considering the last 115 Ma. They conclude that the relationship between GMDST and Antarctic winter SST depends on the location of deepwater formation, and the strength of the overturning circulation. Furthermore, the relationship between Antarctic winter SST and GMSAT depends on the strength of ice albedo feedbacks. As a result, the combined relationship between GMDST and GMSAT changes over the Phanerozoic due to differences in climate state.

Our analysis is based on long model simulations, however some of the simulations have not reached full energy equilibrium yet. Model intercomparison

projects like DeepMIP provide a solid basis for an array of analyses of the simulated climate. Striving for energy equilibrium in the model simulations performed within the standardized boundary conditions of intercomparison projects is necessary for the in-depth analysis of the role of the deep-sea in the climate system. Hence, millennia-long model simulations, ideally ran to full equilibrium, are indispensable for an accurate analysis of the relationship between deep-sea and surface temperatures and a strong test of the assumptions of Hansen et al. (2013).

5.3 Consequences for GMSST, GMSAT, and Climate Sensitivity estimates

Our analysis of the EECO climate based on model-simulations shows a strong linear relationship between GMDST, GMSST, and GMSAT during EECO. The model-based relationships obtained though linear regression can be used together with a proxy-based temperature estimate to translate this temperature estimate into estimates of the other two global temperature indicators. Recent Δ_{47} analysis shows that the paleo-proxy range for the GMDST during EECO is 17 – 20 °C (Meckler et al., 2022), which aligns well with the model-based GMDST estimates of the $6xCO_2$ simulations. We used this proxy-based GMDST range as input to derive estimated ranges of GMSST and GMSAT. Combining the linear relationship between GMDST and GMSST based on only the EECO simulations together with the Δ_{47} GMDST range, we obtain a range for GMSST of 32.8 – 35.3 °C. The linear regression based on both the EECO simulations and the preindustrial control runs leads to a GMSST range of 33.4 – 36.2 °C. These ranges show good agreement with our derived proxy-based GMSST estimate of 31.5 – 35.7 °C. This indicates that the model-based linear relationship is consistent with the combination of proxy-based GMDST and GMSST estimates. Repeating this calculation for GMSAT gives temperature ranges of 30.87 – 33.84 °C (EECO only regression) and 31.40 – 34.67 °C (EECO and PI regressions). Both estimates are high compared to our proxy-based GMSAT estimate of 24.7 – 30.4 °C and the best-estimate of 27.0 °C of Inglis et el. (2020) but align well with our GMSAT estimate based on marine proxies only (31.0 – 35.0 °C) and the upper end of the range 29 ± 3 °C by Zhu et al. (2019).

We used the Δ_{47}-estimate of GMDST from Meckler et al. (2022) because clumped isotope analysis has the advantage that no assumption needs to be made regarding the [18]O of seawater, unlike [18]O analysis (Eiler, 2007; Ghosh et al., 2006). The estimated GMDST for EECO is several degrees higher than the range of 12 – 14 °C based on previous [18]O estimates (e.g., Hansen et al., 2013; Cramer et al., 2011). Note that Meckler et al. (2022) estimated DST for the North-Atlantic, which has a slightly higher mean DST in the DeepMIP model simulations. However, the difference between basin mean and global mean DST is limited (Figure 4), indicating that the estimate of Meckler et al. (2022) could be regarded as representative of GMDST during EECO. Additional clumped isotope reconstructions of DST from other ocean basins will need to confirm this in the future. Note that the inter-basin [18]O isotopic differences were at most 0.5‰ during the EECO, corresponding to a DST variability of at

most 2 °C (see section 5.1; Cramer et al. 2009).

The correspondence between the regression-derived and proxy-based estimates of GMSST indicates that there is model-data agreement regarding seawater temperatures. On the other hand, the GMSAT estimates inferred from the regression relationship are on the higher end of the proxy-based estimates of GMSAT. Note that there is still considerable uncertainty in the estimation of GMSAT from proxies, the outcome varies both with the proxies taken into account and the methodology to deduce a global mean from the local proxies. The first is shown by the difference in our estimates of GMSAT based on both the terrestrial and marine proxies (24.7 – 30.4 °C) and only the marine proxies (31.0 – 35.0 °C). The analysis of Inglis et al. (2020) exemplifies the dependence on methodology: the best-estimate GMSAT is based on six different methods, with underlying best estimates ranges from a low of 22.8 °C to a high of 29.8 °C. Our regression-based estimated GMSAT inferred from recent Δ_{47}-estimates of GMDST could indicate that GMSAT during EECO was higher than previous estimates based on paleothermometers such as ^{18}O.

The regression-inferred GMSAT range of 30.87 – 33.84 °C (based on EECO only regressions) can be used as a starting point to estimate the Equilibrium Climate Sensitivity (ECS) during the EECO, together with estimates of preindustrial GMSAT and CO_2 concentration for both EECO and the preindustrial. ECS is defined as the equilibrium change in GMSAT that results from the change in radiative forcing following a doubling of the atmospheric CO_2 concentration. Note that estimating ECS from two different geological times such as the EECO and the PI has its caveats. Non-CO_2 climate forcings that are different between the EECO and PI, like continental configuration, ice sheets and orbital parameters, need to be corrected for. The same holds for the effects of slow climate feedbacks associated with for example vegetation and ice sheets that are not part of the ECS definition (Sherwood et al., 2020). Following Inglis et al. (2020), we account for non-CO_2 climate forcings and slow feedbacks by deducting a value of 4.5 °C from the GMSAT of EECO. This value is based on a comparison of model simulations for EECO and PI, both with 280 ppm CO_2 concentration by Zhu et al. (2019). Hence, the equilibrium change in GMSAT between EECO and PI due to the difference in CO_2 concentration is calculated as:

$$\text{GMSAT}_{EECO-PI} = \text{GMSAT} \left(\text{EECO}\right)_{\text{EECO}} - 4.5 - \text{GMSAT}_{\text{PI}} \; in \; °C. \quad (3)$$

The change in climate forcing F between EECO and PI due to the difference in CO_2 concentration C follows from the radiative forcing equations of Byrne and Goldblatt (2014):

$$F_{EECO-PI} = 5.32 \bullet \ln\left(\frac{C_{\text{EECO}}}{C_{\text{PI}}}\right) + 0.39 \bullet \left(\ln\left(\frac{C_{\text{EECO}}}{C_{\text{PI}}}\right)\right)^2 \; in \; \frac{W}{m^2}. \quad (4)$$

Applying Equation (4) with a CO_2 concentration ratio $\frac{C_{\text{EECO}}}{C_{\text{PI}}} = 2$ amounts to 3.875, which is the multiplication factor required to translate the outcome into the effect of a CO_2 doubling:

$$\text{ECS}_{EECO-PI} = 3.875 \bullet \frac{\text{GMSAT}_{EECO-PI}}{F_{EECO-PI}}. \quad (5)$$

Assuming a preindustrial GMSAT of 14 °C (as in Inglis et al., 2021), an EECO GMSAT of 30.87 – 33.84 °C, a preindustrial CO_2 level of 280 ppm, and an EECO best estimate CO_2 level of 1,500 ppm (Anagnostou et al., 2020; Rae et al., 2021), we arrive at an ECS estimates of 4.8 – 5.9 °C. Note that this range is directly based on the range in EECO GMSAT and does not take into account uncertainties in the other variables, most importantly the range in the EECO atmospheric CO_2 level of 1,150 – 2,000 ppm (Anagnostou et al., 2020; Rae et al., 2021). Using a 1,150 ppm CO_2 level gives an ECS range of 5.8 – 7.2 °C, and the 2,000 ppm CO_2 level results in a range of 4.0 – 5.0 °C. The obtained ECS estimate (4.8 – 5.9 °C) is higher than the EECO best estimate of Inglis et al. (2021) of 3.1°C, which is a direct consequence of their use of a lower GMSAT estimate (27 °C). An alternative model-based estimate of ECS can be obtained by considering the slope of a linear regression between $\ln(CO_2)$ and the GMSAT relative to PI of the DeepMIP simulations (Figure 2). Considering all models except INMCM, the regression slope is 5.93 with 95% confidence interval of 4.05 – 7.80 ($R^2 = 0.65$). This means that the change in GMSAT is 5.92 °C per unit change in $\ln(CO_2)$, or an ECS estimate of 4.11 (2.81 – 5.41) °C per CO_2 doubling.

By definition, the estimated ECS is highly dependent on the estimates of GMSAT and CO_2 concentration. Hence, constraining temperature and CO_2 estimates of key geologic intervals is a necessity for an accurate estimation of ECS. A reconsideration of the GMDST during EECO based on the latest insights from clumped isotope analysis affects the GMSAT estimate, and hence the ECS estimate. Assuming a fixed CO_2 concentration, a higher GMSAT directly results in a higher ECS. Previous high model-based estimates of ECS from CMIP6 were considered unrealistic based on a comparison of model-based and proxy-based estimates of EECO CO_2 level and GMSAT (Zhu et al., 2002). Our higher GMSAT estimate leads to ECS estimates closer to those of the high-end ECS CMIP6 models. Hence, we argue that paleo-data does not completely rule out the possibility that the high ECS model estimates are realistic. We note that our ECS EECO estimate is higher than the ECS estimate of IPCC AR6 of 3°C for the current climate and lies beyond the likely range of 2.5 – 4.0 °C (Forster et al., 2021). However, it is important to note that estimates of ECS for paleoclimates like the EECO cannot be regarded as directly representative of ECS in our current climate due to the possible climate-state dependence of ECS (Sherwood et al., 2020).

5.4 Outlook into future climate

A good understanding of the EECO climate is highly relevant today, since the atmospheric CO_2 concentration during the 22nd century will be like that of the EECO in the high-emission SSP5-8.5 scenario. Reconstructions of the EECO climate improve our understanding of the workings of the climate system in hothouse conditions such as those possible in the far future. We can regard the linear relationships between GMDST, GMSST, and GMSAT (Figure 5) as time-lines showing the progression of the global mean temperatures under conditions of increasing atmospheric CO_2 concentrations in an ice-free world with EECO continental configuration and vegetation. An interesting subject of future research would be to construct similar timelines for the future under different scenarios of CO_2 emissions. For such research, an understanding of the differences between the EECO and the present climate is necessary.

An essential step for a good comparison of a specific paleoclimate such as the EECO to the climate of the future is an understanding of the impact of differences in non-CO_2 related conditions on the climate system. Through various feedbacks working on different timescales, factors such as vegetation type, continental configuration, and the presence of ice sheets play a role in determining temperatures independent of the atmospheric CO_2 level, as can be seen from the differences between the $1xCO_2$ EECO run and the PI control run. For GMDST, GMSST, and GMSAT, the average differences are 2.1 °C, 3.5 °C, and 3.8 °C respectively. This implies that the response of surface temperatures to non-CO_2 climatic factors seems stronger than that of GMDST. This can be the result of differences in land elevation and the geographical location of the continents. Furthermore, the response of GMDST could be dampened due to the PI value of GMDST being close to freezing point. In the current warming climate, the response of GMDST to non-CO_2 factors could therefore be higher than the model simulations suggest. Additionally, the deep ocean will take millennia to equilibrate to the level of atmospheric CO_2 to be reached in the future. This is a caveat when comparing an equilibrated hothouse climate state like the EECO with the climate of the 22nd century that is still in the progress of obtaining an energy equilibrium.

The above considerations are important when applying knowledge of paleoclimate to the climate of the possible long-term future under high CO_2 conditions. No past hothouse climate is a perfect match for the future climate system. The study of an array of paleoclimates under a wide range of climate forcing conditions is essential to gain an understanding of the workings of the climate system in different underlying situations. Our main finding is the existence of a strong linear relationship between GMDST, GMSST, and GMSAT during the high atmospheric CO_2 conditions of the EECO, but this relationship does not necessary translate 1-to-1 to other past and future climates. In order to use this relationship in a broader context, it is important to determine to which degree the relationship is specific to the climate state of the EECO as implemented in the model simulations. The robustness of the found relationships can be tested on other warm climate states such as the Mid-Pliocene Warm Period (MPWP; 3.3 - 3.0 Ma) and the Miocene Climate Optimum (MCO; 16.9 – 14.7 Ma). These

geologic intervals are characterized by more moderate atmospheric CO_2 levels and warming compared to the EECO: the atmospheric CO_2 level during the MPWP was comparable to today and MCO CO_2 levels were approximately 600 – 800 ppm (Figure 1; Rae et al., 2021). The MPWP is the key geologic interval to gain understanding of the 21st century climate system under scenario SSP2-4.5 (Burke et al., 2018), which incorporates planned mitigation and adaptation actions by national governments (Chen et al., 2021). The atmospheric CO_2 level of the MCO is comparable to the projected CO_2 level in 2100 under the SSP3-7.0 scenario (Figure 1), which is an intermediate-to-high emission scenario (Chen et al., 2021). The Model Intercomparison Projects PlioMIP for the MPWP (Haywood et al., 2021), and MioMIP for the MCO (Burls et al., 2021) provide an opportunity to expand our analysis of the relationship between temperatures in the deep-sea and temperatures at the surface to these warm paleoclimates.

6 Conclusion

Using millennia-long model runs simulating the Early Eocene Climate Optimum, we have investigated the long-term responses of global mean deep-sea temperature, sea-surface temperature, and surface air temperature to different atmospheric CO_2 levels. The model simulations show limited spatial variability in DST, indicating that local DST estimates can be regarded as reasonably representative of GMDST. We estimate a strong linear relationship between GMDST and both GMSST and GMSAT for the different EECO simulations using linear regression. The results indicate that GMDST responds more strongly to changes in atmospheric CO_2 than GMSST by a factor 1.18. Furthermore, GMSAT is more sensitive to CO_2 changes than GMSST by a factor 1.17. Hence, the responses of GMDST and GMSAT to atmospheric CO_2 changes are similar in magnitude. This indicates that changes in GMDST can be used to estimate changes in GMSAT, validating the assumptions made by Hansen et al. (2013) for the DeepMIP EECO model simulations.

To make a model-data comparison, we derived a proxy-based GMSST of 33.7 °C (95% CI: 31.5 – 35.7), a GMSAT estimate of 27.3 °C (95% CI: 24.7 – 30.4) based on marine and terrestrial paleo proxies, and of 33.1 °C (95% CI: 31.0 – 35.0), based on marine proxies only. Furthermore, Inglis et al. (2020) derived a proxy-based best estimate for GMSAT of 27.0 °C (95% CI: 17.5 – 35.9), and Zhu et al. (2019) arrive at an estimate of 29 ± 3 °C (95% CI). Finally, recent Δ_{47} analysis indicates that GMDST during the EECO was 17-20 °C (Meckler et al., 2022). The best fit of these paleo proxy estimates is found with the 6xCO_2 model simulations. The corresponding CO_2 level of 1,680 ppm is also in agreement with paleo proxies of atmospheric CO_2 during EECO of 1,150 – 2,000 ppm (Anagnostou et al., 2020; Rae et al., 2021). Hence, the model simulations align well with paleo proxies in their combination of CO_2 level, GMDST, GMSST, and GMSAT. Further research into other Cenozoic climate states is needed to test the robustness of these results. Such an improved understanding of past climates is indispensable today to better understand the changing climate of the future.

Open Research

The research was performed using model data output from the Deep-Time Model Intercomparison Project (DeepMIP; Lunt et al., 2021). Access to the DeepMIP model database can be requested from the project team via deepmip.org. The dataset of local SST and SAT proxy estimates used in the analysis was obtained from the supplementary information of (Inglis et al., 2020). The datasets on modern ocean temperatures were obtained from E.U. Copernicus Marine Service Information (2021a; 2021b; 2021c). Hersbach et al. (2019) was downloaded from the Copernicus Climate Change Service (C3S) Climate Data Store.

Supplement

The supplement related to this article is available online at: <to be filled in>.

Acknowledgments

References

Anagnostou, E., John, E. H., Babila, T. L., Sexton, P. F., Ridgwell, A., Lunt, D. J., Pearson, P. N., Chalk, T. B., Pancost, R. D., & Foster, G. L. (2020). Proxy evidence for state-dependence of climate sensitivity in the Eocene greenhouse. *Nature Communications*, *11*(1). https://doi.org/10.1038/s41467-020-17887-x

Baatsen, M., Von der Heydt, A. S., Huber, M., Kliphuis, M. A., Bijl, P. K., Sluijs, A. & Dijkstra, H. A. (2020). The middle to late Eocene greenhouse climate modelled using the CESM 1.0.5. *Climate of the Past*, 16(6), 2573-2597. https://doi.org/10.5194/cp-16-2573-2020

Burke, K. D., Williams, J. W., Chandler, M. A., Haywood, A. M., Lunt, D. J., & Otto-Bliesner, B. L. (2018). Pliocene and Eocene provide best analogs for near-future climates. *Proceedings of the National Academy of Sciences of the United States of America*, *115*(52), 13288–13293. https://doi.org/10.1073/pnas.1809600115

Burls, N. J., Bradshaw, C. D., De Boer, A. M., Herold, N., Huber, M., Pound, M., Donnadieu, Y., Farnsworth, A., Frigola, A., Gasson, E., Von der Heydt, A. S., Hutchinson, D. K., Knorr, G., Lawrence, K. T., Lear, C. H., Li, X., Lohmann, G., Lunt, D. J., Marzocchi, A., Prange, M., Riihimaki, C.A., Sarr, A.-C., Siler, N., & Zhang, Z. (2021). Simulating Miocene Warmth: Insights from an Opportunistic Multi-Model Ensemble (MioMIP1). *Paleoceanography and Paleoclimatology*, *36*(5). https://doi.org/10.1029/2020PA004054

Byrne, B., & Goldblatt, C. (2014). Radiative forcing at high concentrations of well-mixed greenhouse gases. *Geophysical Research Letters,* 41(1), 152–160. https://doi.org/10.1002/2013GL058456

Chen, D., M. Rojas, B. H. Samset, K. Cobb, A. Diongue Niang, P. Edwards, S. Emori, S. H. Faria, E. Hawkins, P. Hope, P. Huybrechts, M. Meinshausen, S. K. Mustafa, G. K. Plattner, & A. M. Tréguier. (2021). Framing, Context, and Methods. In V. Masson-Delmotte, P. Zhai, A. Pirani, S. L. Connors, C. Péan, S. Berger, N. Caud, Y. Chen, L. Goldfarb, M. I. Gomis, M. Huang, K. Leitzell, E. Lonnoy, J. B. R. Matthews, T. K. Maycock, T. Waterfield, O. Yelekçi, & B. Z. R. Yu (Eds.), *Climate Change 2021: The Physical Science Basis. Contribution of Working Group I to the Sixth Assessment Report of the Intergovernmental Panel on Climate Change.* Cambridge University Press, Cambridge, United Kingdom and New York, NY, USA, 147–286.

Cramer, B. S., Toggweiler, J. R., Wright, J. D., Katz, M. E., & Miller, K. G. (2009). Ocean overturning since the Late Cretaceous: Inferences from

a new benthic foraminiferal isotope compilation. *Paleoceanography*, 24(4). https://doi.org/10.1029/2008PA001683

Cramer, B. S., Miller, K. G., Barrett, P. J., & Wright, J. D. (2011). Late Cretaceous-Neogene trends in deep ocean temperature and continental ice volume: Reconciling records of benthic foraminiferal geochemistry (^{18}O and Mg/Ca) with sea level history. *Journal of Geophysical Research: Oceans*, 116(12). https://doi.org/10.1029/2011JC007255

Desbruyères, D. G., Purkey, S. G., McDonagh, E. L., Johnson, G. C., & King, B. A. (2016). Deep and abyssal ocean warming from 35 years of repeat hydrography. *Geophysical Research Letters*, 43(19), 10,356-10,365. https://doi.org/10.1002/2016GL070413

Eiler, J. M. (2007). "Clumped-isotope" geochemistry-The study of naturally-occurring, multiply-substituted isotopologues. *Earth and Planetary Science Letters*, 262(3–4), 309–327. https://doi.org/10.1016/j.epsl.2007.08.020

E.U. Copernicus Marine Service Information. (2021a). *Global Ocean OSTIA Sea Surface Temperature and Sea Ice Analysis*. https://doi.org/10.48670/moi-00165

E.U. Copernicus Marine Service Information. (2021b). *Global Ocean Physical Reanalysis dataset*. https://doi.org/10.48670/moi-00021

E.U. Copernicus Marine Service Information. (2021c). *Multi Observation Global Ocean ARMOR3D Temperature dataset*. https://doi.org/10.48670/moi-00052

Farnsworth, A., Lunt, D., O'Brien, C., Foster, G., Inglis, G., Markwick, P., Pancost, R., and Robinson, S. (2019). Climate sensitivity on geological timescales controlled by nonlinear feedbacks and ocean circulation, *Geophysical Research Letters*, 46 (16), 9880–9889. https://doi.org/10.1029/2019GL083574

Forster, P., T. Storelvmo, K. Armour, W. Collins, J. L. Dufresne, D. Frame, D. J. Lunt, T. Mauritsen, M. D. Palmer, M. Watanabe, M. Wild, & H. Zhang. (2021). The Earth's Energy Budget, Climate Feedbacks, and Climate Sensitivity. In V. Masson-Delmotte, P. Zhai, A. Pirani, S. L. Connors, C. Péan, S. Berger, N. Caud, Y. Chen, L. Goldfarb, M. I. Gomis, M. Huang, K. Leitzell, E. Lonnoy, J. B. R. Matthews, T. K. Maycock, T. Waterfield, O. Yelekçi, R. Yu, & B. Zhou (Eds.), *Climate Change 2021: The Physical Science Basis. Contribution of Working Group I to the Sixth Assessment Report of the Intergovernmental Panel on Climate Change*. Cambridge University Press, Cambridge, United Kingdom and New York, NY, USA, 923-1054.

Ghosh, P., Adkins, J., Affek, H., Balta, B., Guo, W., Schauble, E. A., Schrag, D., & Eiler, J. M. (2006). ^{13}C-^{18}O bonds in carbonate minerals: A new kind of paleothermometer. *Geochimica et Cosmochimica Acta*, 70(6), 1439–1456. https://doi.org/10.1016/j.gca.2005.11.014

Gulev, S. K., P. W. Thorne, J. Ahn, F. J. Dentener, C. M. Domingues, S. Gerland, D. Gong, D. S. Kaufman, H. C. Nnamchi, J. Quaas, J. A. Rivera, S. Sathyendranath, S. L. Smith, B. Trewin, K. von Shuckmann, & R. S. Vose.

(2021). Changing State of the Climate System. In V. Masson- Delmotte, P. Zhai, A. Pirani, S. L. Connors, C. Péan, S. Berger, N. Caud, Y. Chen, L. Goldfarb, M. I. Gomis, M. Huang, K. Leitzell, E. Lonnoy, J. B. R. Matthews, T. K. Maycock, T. Waterfield, O. Yelekçi, R. Yu, & B. Zhou (Eds.), *Climate Change 2021: The Physical Science Basis. Contribution of Working Group I to the Sixth Assessment Report of the Intergovernmental Panel on Climate Change.* Cambridge University Press, Cambridge, United Kingdom and New York, NY, USA, 287–422.

Hansen, J., Sato, M., Russell, G., & Kharecha, P. (2013). Climate sensitivity, sea level and atmospheric carbon dioxide. *Philosophical Transactions of the Royal Society A: Mathematical, Physical and Engineering Sciences*, *371*(2001). https://doi.org/10.1098/rsta.2012.0294

Haywood, A. M., Dowsett, H. J., Tindall, J. C., PlioMIP1 participants, & PlioMIP2 participants. (2021). PlioMIP: The Pliocene Model Intercomparison Project. *Past Global Changes Magazine*, *29*(2), 92–93. https://doi.org/10.22498/pages.29.2.92

Hersbach, H., Bell, B., Berrisford, P., Biavati, G., Horányi, A., Muñoz Sabater, J., Nicolas, J., Peubey, C., Radu, R., Rozum, I., Schepers, D., Simmons, A., Soci, C., Dee, D., Thépaut, J-N. (2019): ERA5 monthly averaged data on single levels from 1959 to present. *Copernicus Climate Change Service (C3S) Climate Data Store (CDS)*. (Accessed on 31-01-2022), 10.24381/cds.f17050d7

Hollis, C. J., Dunkley Jones, T., Anagnostou, E., Bijl, P. K., Cramwinckel, M. J., Cui, Y., Dickens, G. R., Edgar, K. M., Eley, Y., Evans, D., Foster, G. L., Frieling, J., Inglis, G. N., Kennedy, E. M., Kozdon, R., Lauretano, V., Lear, C. H., Littler, K., Lourens, L., Meckler, A.N., Naafs, B.D.A., Pälike, H., Pancost, R.D., Pearson, P.N., Röhl, U., Royer, D.L., Salzmann, U., Schubert, B.A., Seebeck, H., Sluijs, A., Speijer, R.P., Stassen, P., Tierney, J., Tripati, A., Wade, B., Westerhold, T., Witkowski, C., Zachos, J.C., Zhang, Y.G., Huber, M., & Lunt, D. J. (2019). The DeepMIP contribution to PMIP4: Methodologies for selection, compilation and analysis of latest Paleocene and early Eocene climate proxy data, incorporating version 0.1 of the DeepMIP database. *Geoscientific Model Development*, *12*(7), 3149–3206. https://doi.org/10.5194/gmd-12-3149-2019

Inglis, G. N., Bragg, F., Burls, N. J., Cramwinckel, M. J., Evans, D., Foster, G. L., Huber, M., Lunt, D. J., Siler, N., Steinig, S., Tierney, J. E., Wilkinson, R., Anagnostou, E., De Boer, A. M., Dunkley Jones, T., Edgar, K. M., Hollis, C. J., Hutchinson, D. K., & Pancost, R. D. 2020). Global mean surface temperature and climate sensitivity of the EECO, PETM and latest Paleocene. *Climate of The Past Discussions*, *16*(5). https://doi.org/10.5194/cp-16-1953-2020.

Kim, S-T, & O'Neil, J. R. (1997). Equilibrium and nonequilibrium oxygen isotope effects in synthetic carbonates. Geochimica et Cosmochimica Acta, 61(16), 3461–3475. https://doi.org/10.1016/S0016-7037(97)00169-5.

Li, C., von Storch, J. S., & Marotzke, J. (2013). Deep-ocean heat uptake

and equilibrium climate response. *Climate Dynamics*, *40*(5–6), 1071–1086. https://doi.org/10.1007/s00382-012-1350-z

Lunt, D. J., Bragg, F., Chan, W.-L., Hutchinson, D., Ladant, J.-B., Morozova, P., Niezgodzki, I., Steinig, S., Zhang, Z., Zhu, J., Abe-Ouchi, A., Anagnostou, E., De Boer, A. M., Coxall, H. K., Donnadieu, Y., Foster, G., Inglis, G. N., Knorr, G., Langebroek, P. M., Lear, C. H., Lohmann, G., Poulsen, C. J., Sepulchre, P., Tierney, J. E., Valdes, P. J., Volodin, E. M., Dunkley Jones, T., Hollis, C. J., Huber, M., & Otto-Bliesner, B. L.. (2021). DeepMIP: Model intercomparison of early Eocene climatic optimum (EECO) large-scale climate features and comparison with proxy data. *Climate of The Past Discussions*, *17*(1). https://doi.org/10.5194/cp-17-203-2021

Lunt, D. J., Dunkley Jones, T., Heinemann, M., Huber, M., LeGrande, A., Winguth, A., Loptson, C., Marotzke, J., Roberts, C. D., Tindall, J., Valdes, P. and Winguth, C. (2012). A model–data comparison for a multi-model ensemble of early Eocene atmosphere–ocean simulations: EoMIP. *Climate of the Past*, 8(5), 1717-1736. https://doi.org/10.5194/cp-8-1717-2012

Lunt, D. J., Huber, M., Anagnostou, E., Baatsen, M. L. J., Caballero, R., DeConto, R., Dijkstra, H. A., Donnadieu, Y., Evans, D., Feng, R., Foster, G. L., Gasson, E., Von der Heydt, A. S., Hollis, C. J., Inglis, G. N., Jones, S. M., Kiehl, J., Kirtland Turner, S. K., Korty, R. L., Kozdon, R., Krishnan, S., Ladant, J.-B., Langebroek, P., Lear, C.H., LeGrande, A.N., Littler, K., Markwick, P., Otto-Bliesner, B., Pearson, P., Poulsen, C.J., Salzmann, U., Shields, C., Snell, K., Stärz, M., Super, J., Tabor, C., Tierney, J.E., Tourte, G.J.L., Tripati, A., Upchurch, G.R., Wade, B.S., Wing, S.L., Winguth, A.M.E., Wright, N.M., Zachos, J.C., & Zeebe, R. E. (2017). The DeepMIP contribution to PMIP4: Experimental design for model simulations of the EECO, PETM, and pre-PETM (version 1.0). *Geoscientific Model Development*, *10*(2), 889–901. https://doi.org/10.5194/gmd-10-889-2017

McCrea, J. M. (1950). On the Isotopic Chemistry of Carbonates and a Paleotemperature Scale. *The Journal of Chemical Physics*, *18*(6), 849–857. https://doi.org/10.1063/1.1747785

Meckler, A. N., Sexton, P., Piasecki, A. M., Leutert, T., Marquardt, J., Ziegler, M., Agterhuis, T., Lourens, L. J., Rae, J. W. B., Barnet, J., Tripati, A., & Bernasconi, S. M. (2022). *Cenozoic evolution of deep-sea temperature from clumped isotope thermometry.* Science, 377(6601), 86-90. https://www.science.org/doi/10.1126/science.abk0604

NOAA. (2021). *Despite pandemic shutdowns, carbon dioxide and methane surged in 2020.* Retrieved May 27, 2022, from https://research.noaa.gov/article/ArtMID/587/ArticleID/2742/I

Pross, J., Contreras, L., Bijl, P. K., Greenwood, D. R., Bohaty, S. M., Schouten, S., Bendle, J. A., Röhl, U., Tauxe, L., Raine, J. I., Huck, C. E., Van de Flierdt, T., Jamieson, S. S. R., Stickley, C. E., Van de Schootbrugge, B., Escutia, C., Brinkhuis, H., & Integrated Ocean Drilling Program Expedition 318 Scientists

(2012). Persistent near–tropical warmth on the antarctic continent during the early eocene epoch. *Nature, 488*(7409), 73–77. https://doi.org/10.1038/nature 11300

Rae, J. W. B., Zhang, Y. G., Liu, X., Foster, G. L., Stoll, H. M., & Whiteford, R. D. M. (2021). Atmospheric CO_2 over the Past 66 Million Years from Marine Archives. *The Annual Review of Earth and Planetary Sciences, 49*, 609–641. https://doi.org/10.1146/annurev-earth-082420-063026

Sauermilch, I., Whittaker, J. M., Klocker, A., Munday, D. R., Hochmuth, K., Bijl, P. K., & LaCasce, J. H. (2021). Gateway-driven weakening of ocean gyres leads to Southern Ocean cooling. *Nature Communications, 12*(1). https://doi.org/10.1038/s41467-021-26658-1

Sherwood, S. C., Webb, M. J., Annan, J. D., Armour, K. C., Forster, P. M., Hargreaves, J. C., Hegerl, G., Klein, S. A., Marvel, K. D., Rohling, E. J., Watanabe, M., Andrews, T., Braconnot, P., Bretherton, C. S., Foster, G. L., Hausfather, Z., von der Heydt, A. S., Knutti, R., Mauritsen, T., Norris, J. R., Proistosescu, C., Rugenstein, M., Schmidt, G. A., Tokarska, K. B., Zelinka, M. D. (2020). An Assessment of Earth's Climate Sensitivity Using Multiple Lines of Evidence. *Reviews of Geophysics,* 58(4). https://doi.org/10.1029/2019RG000678

Sijp, W. P., England, M. H., & Huber, M. (2011). Effect of the deepening of the Tasman Gateway on the global ocean. *Paleoceanography, 26*(4). https://doi.org/10.1029/2011PA002143

Stevens, B., Giorgetta, M., Esch, M., Mauritsen, T., Crueger, T., Rast, S., Salzmann, M., Schmidt, H., Bader, J., Block, K., Borkopf, R., Fast, I., Kinne, S., Kornblueh, L., Lohmann, U., Pincus, R., Reichler, T., & Roeckner, E. (2013). Atmospheric component of the MPI-M Earth System Model: ECHAM6. *Journal of Advances in Modeling Earth Systems*, 5(2), 146–172, https://doi.org/10.1002/jame.20015

Tierney, J., Poulsen, C., Montañez, I., Bhattacharya, T., Feng, R., Ford, H., Hönisch, B., Inglis, G., Petersen, S., Sagoo, N., Tabor, C., Thirumalai, K., Zhu, J., Burls, N., Foster, G., Goddéris, Y., Huber, B., Ivany, L., Kirtland Turner, S., Lunt, D.J., McElwain, J.C., Mills, B.J.W., Otto-Bliesner, B.L., Ridgwell, A., & Zhang, Y. (2020). Past climates inform our future. *Science, 370*(6517). https://doi.org/10.1126/science.aay3701

The University of Melbourne. (n.d.). *Greenhouse Gas Factsheets.* Retrieved September 20, 2021, from https://greenhousegases.science.unimelb.edu.au/

Urey, H. C. (1948). Oxygen Isotopes in Nature and in the Laboratory. *Science, New Series,* 108(2810). https://doi:10.1126/science.108.2810.489

Valdes, P., Scotese, C., & Lunt, D. (2020). Deep Ocean Temperatures through Time. *Climate of the Past*, 17(4), 1483-1506. https://doi.org/10.5194/cp-17-1483-2021

Westerhold, T., Marwan, N., Drury, A. J., Liebrand, D., Agnini, C., Anagnostou, E., Barnet, J. S. K., Bohaty, S. M., de Vleeschouwer, D., Florindo, F.,

Frederichs, T., Hodell, D. A., Holbourn, A. E., Kroon, D., Lauretano, V., Littler, K., Lourens, L. J., Lyle, M., Pälike, H., Röhl, U., Tian, J., Wilkens, R. H., Wilson, P. A., Zachos, J. C. (2020). An astronomically dated record of Earth's climate and its predictability over the last 66 million years. *Science*, *369*(6509), 1383–1387. https://doi.org/10.1126/science.aba6853

Zachos, J.C., Pagani, M.O., Sloan, L.C., Thomas, E. & Billups, K. (2001). Trends, Rhythms, and Aberrations in Global Climate 65 Ma to Present. *Science*, 292, 686-93. https://doi.org/10.1126/science.1059412

Zhang, Y., de Boer, A. M., Lunt, D. J., Hutchinson, D. K., Ross, P., van de Flierdt, T., Sexton, P., Coxall, H. K., Steinig, S., Ladant, J.-B., Zhu, J., Donnadieu, Y., Zhang, Z., Chan, W.-L., Abe-Ouchi, A., Niezgodzki, I., Lohmann, G., Knorr, G., Poulsen, C. J., & Huber, M. (2022). Early Eocene ocean meridional overturning circulation: the roles of atmospheric forcing and strait geometry. *Paleoceanography and Paleoclimatology 37(3).* https://doi.org/10.1029/2021pa004329

Zhang, Y., Huck, T., Lique, C., Donnadieu, Y., Ladant, J.-B., Rabineau, M., & Aslanian, D. (2020). Early Eocene vigorous ocean overturning and its contribution to a warm Southern Ocean. *Climate of The Past Discussions*, 16, 1–35. https://doi.org/10.5194/cp-2019-163

Zhu, J., Poulsen, C. J., & Tierney, J. E. (2019). Simulation of Eocene extreme warmth and high climate sensitivity through cloud feedbacks. *Science Advances*, *5*(9), 1–11. https://doi.org/10.1126/sciadv.aax1874

Zhu, J., Poulsen, C. J., Otto-Bliesner, B. L. (2020). High climate sensitivity in CMIP6 model not supported by paleoclimate. *Nature Climate Change*, 10(5), 378–379. https://doi.org/10.1038/s41558-020-0764-6